CrossMark

J. Fluid Mech. (2018), *vol.* 847, *pp.* 552–590. © Cambridge University Press 2018
doi:10.1017/jfm.2018.314

Influence of permeable beds on hydraulically macro-rough flow

Hongwei Fang[1], Xu Han[1], Guojian He[1,†] and Subhasish Dey[2]

[1]State Key Laboratory of Hydro-science and Engineering, Department of Hydraulic Engineering, Tsinghua University, Beijing 100084, China

[2]Department of Civil Engineering, Indian Institute of Technology Kharagpur, West Bengal 721302, India

(Received 1 July 2017; revised 29 March 2018; accepted 11 April 2018; first published online 25 May 2018)

In this study, macro-rough flows over beds with different permeability values are simulated using the large-eddy simulation, and the results are analysed by applying the double-averaging (DA) methodology. Spheres of different sizes and arrangements were used to form the beds, which are deemed to be permeable granular beds. The influence of bed permeability on the turbulence dynamics and structure is investigated. It was observed that the scales of the spanwise vortical structures over more permeable beds are larger than those over less permeable beds. This is attributed to large-scale spanwise-alternate strips of varying Reynolds shear stress (RSS), emerging from the surface of macro-rough elements for the permeable beds. The DA stress balance suggests that the time-averaged spanwise vortical structure leads to a damping in DA RSS and an unusual peak of the form-induced stress in the main flow. In the streamwise direction, both large turbulent structures that originate from the Kelvin–Helmholtz-type instability and small turbulent structures that are associated with the turbulent transport across the gaps of the roughness elements are more prevalent over highly permeable beds. Near the bed, the relative magnitude of turbulent events shows a transition from a ejections-dominating to sweeps-dominating zone with vertical distance. Further, several hydrodynamic characteristics normalized by inner scales (kinematic viscosity to shear velocity ratio) show a greater dependency on permeability Reynolds number than those normalized by sediment size. The study provides an insight into the mechanism of mass transfer near the fluid–particle interface, which is vital to benthic and aquatic ecology.

Key words: turbulence simulation, turbulent flows

1. Introduction

Turbulent flow over and within permeable beds is encountered in a wide range of practical situations, including industrial devices and the environmental field. In industry, such a kind of flow is expected to influence the efficiency of catalytic converters and metal foam heat exchangers. In the environmental field, including gravel-bed streams or marine environments, the dispersion of pollutants and the

† Email address for correspondence: heguojian@tsinghua.edu.cn

https://doi.org/10.1017/jfm.2018.314 Published online by Cambridge University Press

exchange of oxygen and nutrients are related to turbulence over riverbeds or sea floors.

As it is an important issue to understand the flow physics over and within permeable beds, several studies have been performed to investigate the influence of permeability on fluid flows. In laminar flow through an open channel, Beavers & Joseph (1967) measured the mass flow rates and found that the frictional resistance over a permeable bed is smaller than that over a smooth (impermeable) bed owing to the effective slip velocity over the permeable bed. On the other hand, in turbulent flow through an open channel, the result was contrary to that for laminar flow. Zagni & Smith (1976) carried out experiments on turbulent flow over permeable channel beds. They found that the frictional resistance in flow over a permeable bed was greater than that over an impermeable bed with the identical surface roughness. Similar results were also obtained by Kong & Schetz (1982) and Zippe & Graf (1983). In addition, Manes *et al.* (2009) conducted particle image velocimetry (PIV) experiments over impermeable and permeable beds made of spheres. They found that effect of the bed permeability is to increase the friction factor even in the hydraulically rough regime. Further experimental studies on flow over permeable beds were also reported by Suga *et al.* (2010), Manes, Poggi & Ridolfi (2011), Suga, Mori & Kaneda (2011) and Suga (2016). They observed that as the permeability increases, the near-wall turbulence structure evolves progressively to a more organized state having an enhancement of the vertical Reynolds normal stress. The dominance of sweeps near the bed and instability of the Kelvin–Helmholtz (KH) type were the possible cause of shortening of the streamwise vortical structures. From these experimental studies, it was revealed that in a turbulent flow, the friction factor increases as a result of the higher Reynolds shear stress (RSS). The RSS, in turn, increases owing to the effects of eddies which originate from the KH-type instability over beds with a high permeability.

However, in laboratory experimental flumes, the velocity measurements were generally taken on a central vertical plane and the spanwise heterogeneity was ignored (Nezu & Nakagawa 1993; Kironoto & Graf 1994; Song & Graf 1994; Nikora & Smart 1997; Nikora & Goring 2000; Dey & Raikar 2007; Smart & Habersack 2007; Amir, Nikora & Stewart 2014; Khosronejad & Sotiropoulos 2014). These studies have enhanced our understanding of complex turbulence phenomena in the context of the time-averaging concept. Nevertheless, knowledge on the turbulence characteristics of hydraulically macro-rough flows over permeable beds is still somewhat subjective because of the highly three-dimensional and large-scale heterogeneous nature of flows near macro-rough beds. To supplement the time-averaging concept, area-averaging in the layer parallel to the mean bed surface is performed for the distribution of the time-averaging values. Thus, a double-averaging methodology (DAM) was introduced. The DAM has so far been extensively applied to study the atmospheric boundary layer (Wilson & Shaw 1977) and gravel-bed streams (Nikora *et al.* 2001, 2007*a*,*b*; Mignot, Barthelemy & Hurther 2009*a*; Mignot, Hurther & Barthelemy 2009*b*; Sarkar & Dey 2010; Dey & Das 2012; Ferraro *et al.* 2016; Sarkar, Papanicolaou & Dey 2016; Han, He & Fang 2017).

To study flows over permeable beds, direct numerical simulation (DNS) is performed by several studies. The simplest method in this regard was to specify the boundary conditions, as was done by Jimenez *et al.* (2001) and Hahn, Je & Choi (2002). They set the vertical velocity component to be zero or proportional to the local pressure fluctuations. However, this approach was not realistic for beds with high permeability, where an exchange of momentum across the bed interface takes place. Breugem, Boersma & Uittenbogaard (2006) applied the

https://doi.org/10.1017/jfm.2018.314 Published online by Cambridge University Press

volume-averaged Navier–Stokes (VANS) equations given by Whitaker (1996) with a Darcy–Forchheimer-type body force to represent the porous medium. They found that fluid streaks and associated quasi-streamwise vortices are absent near the highly permeable bed. Significantly enhanced turbulence is dominant with relatively large vortical structures, which are supposed to originate from an instability of the KH type. They concluded that this process contributes strongly to the RSS and thus leads to a strong frictional resistance. However, since they neglected the effects of dispersion, the turbulence phenomena near and within the permeable bed were not precisely reproduced. Liu & Prosperetti (2011) studied three-dimensional flow in a channel bounded by a permeable wall, which was simulated by spheres in a simple cubic arrangement. They mainly focused on the force and the torque to the sphere layer, but the details of the hydrodynamic quantities and the effects of permeability on them were overlooked. Kuwata & Suga (2016) conducted Lattice Boltzmann DNS simulation for turbulence over interconnected staggered cubic arrays. By proper orthogonal decomposition, they found that the vortex structure over the permeable layer becomes shredded and the pitch of the fluid streaks becomes approximately twice as wide as those over impermeable beds. Instability of the KH type was detected across the channels. Since enormous computational costs were involved to resolve the complex permeable structures at high Reynolds numbers for the DNS, the bulk Reynolds number in their simulation was considered as 3000, which was too far from the Reynolds number obtained in a natural turbulent flow. Although the staggered cubic arrays that they adopted fitted well with the grids, the layers of packed spheres were more likely to simulate a natural sand bed.

To the authors' best knowledge, the study of numerical simulations on turbulence structures at the interface of near-bed flow and permeable beds is limited to relatively low Reynolds numbers. The present study therefore aims to investigate the effects of bed permeability on the turbulent characteristics of macro-rough flow at a high Reynolds number. Large-eddy simulation (LES) of flows over three cases with different permeability values having the identical structure of surface elements was conducted. It may be noted that the results of the impermeable bed are considered as the reference. In addition, the DAM is used to analyse heterogeneous macro-rough flow near macro-rough beds and in the main flow. This study provides new insights into various aspects of turbulence characteristics.

The rest of the paper is organized as follows: the numerical framework is explained in § 2. The numerical experiments and bed configurations are described in § 3. The LES results are presented in § 4. Finally, the summary and conclusions are given in § 5.

2. Problem formulation

2.1. *Numerical framework*

In this study, the second version of a code called LESOCC2 (large-eddy simulation on curvilinear coordinates), which was first developed at the Institute for Hydromechanics, Karlsruhe Institute of Technology, Germany (Breuer & Rodi 1994; Fröhlich & Rodi 2002), was used for the simulations. The dimensionless LES equations obtained by filtering of the incompressible Navier–Stokes equations can be written as

$$\frac{\partial u_i}{\partial x_i} = 0 \tag{2.1}$$

$$\frac{\partial u_i}{\partial t} + \frac{\partial}{\partial x_j}(u_i u_j) = -\frac{\partial p}{\partial x_i} + \frac{\partial}{\partial x_j}\left[\upsilon\left(\frac{\partial u_i}{\partial x_j} + \frac{\partial u_j}{\partial x_i}\right)\right] - \frac{\partial \tau_{ij}^{SGS}}{\partial x_j}, \tag{2.2}$$

https://doi.org/10.1017/jfm.2018.314 Published online by Cambridge University Press

where u_i and u_j are the ith and jth components of the resolved instantaneous velocity vector (i or $j = 1,\ 2,\ 3$), x_1, x_2 and x_3 represent the spatial location vectors in the x, y and z directions, respectively, p is the resolved dimensionless pressure and υ is the coefficient of kinematic viscosity of the fluid. The subgrid scale (SGS) stress τ_{ij}^{SGS} results from filtering of the nonlinear convective fluxes. This term reflects the influence of the subgrid scale turbulence structures on the large eddies. The SGS stress τ_{ij}^{SGS} was calculated through an eddy viscosity relation as

$$\tau_{ij}^{SGS} = -\upsilon_{SGS}\left(\frac{\partial u_i}{\partial x_j} + \frac{\partial u_j}{\partial x_i}\right) + \frac{1}{3}\delta_{ij}\tau_{kk}^{SGS}, \tag{2.3}$$

where the SGS viscosity υ_{SGS} is computed from the dynamic subgrid scale (SGS) model proposed by Germano *et al.* (1991), δ_{ij} is Kronecker delta.

The governing equations were discretized by the finite-volume method on non-staggered curvilinear grids. Since the outer contour of the roughness elements (hemispheres for impermeable bed and spheres for permeable beds) intersected with the grid lines, the direct forcing immersed boundary method (IBM), originally developed by Peskin (1972), was incorporated in the LES model. The details of the discretization and the IBM treatment of LESOCC2 are available in Fang *et al.* (2014).

2.2. *Averaging approach*

The DAM was used to analyse the flows near macro-rough beds. A local instantaneous flow variable θ can be decomposed into the time–space averaging as

$$\theta(x, y, z, t) = \langle\bar{\theta}\rangle(z) + \tilde{\theta}(x, y, z) + \theta'(x, y, z, t), \tag{2.4}$$

where $\tilde{\theta}$ represents the disturbance of the local time-averaged flow parameter $\bar{\theta}$ from the double-averaged (DA) flow parameter $\langle\bar{\theta}\rangle$ (that is, $\tilde{\theta} = \bar{\theta} - \langle\bar{\theta}\rangle$), and θ' is the difference of the local instantaneous flow parameter θ from the local time-averaged flow parameter $\bar{\theta}$ (that is, $\theta' = \theta - \bar{\theta}$). The spatial averaging used in this study is the intrinsic spatial averaging (Nikora *et al.* 2007*a*):

$$\langle\bar{\theta}\rangle(z) = \frac{1}{A_f}\iint_{A_f}\bar{\theta}(x, y, z)\,\mathrm{d}S, \tag{2.5}$$

where A_f is the area occupied by the fluid at elevation z within the total area and $\mathrm{d}S$ is an infinitesimal area element. The area A_f is typically chosen to be much larger than roughness or flow geometry scales, but smaller than larger geometric features, such as channel curvature and widening or narrowing (Coleman *et al.* 2007). Since the DAM is applicable for the near-bed flow over and within the flow-roughness-element interface, it enables us to have an insight into the turbulence characteristics of the flow sublayers induced by roughness elements and their link with the main flow. As shown in figure 1, these flow sublayers are the form-induced and interfacial sublayers, together called the roughness sublayer (Dey & Das 2012). The form-induced sublayer that occupies the flow zone around the roughness crests is influenced by the individual roughness elements. On the other hand, the interfacial sublayer occupies the flow zone below the form-induced sublayer, where skin friction and form drag appear.

The DA momentum conservation equation based on the Navier–Stokes equations was developed by Nikora *et al.* (2001, 2007*a*) using the time–space averaging procedure.

https://doi.org/10.1017/jfm.2018.314 Published online by Cambridge University Press

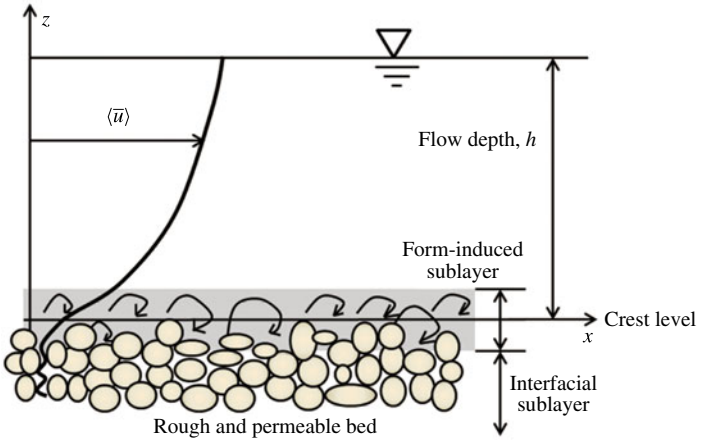

FIGURE 1. (Colour online) Flow over a rough, permeable bed showing the flow sublayers.

For a uniform, two-dimensional open-channel flow (Giménez-Curto & Corniero 2002; Manes, Pokrajac & McEwan 2007; Nikora *et al.* 2007*a*; Dey & Das 2012), the stress balance is given by

$$\langle\bar{\tau}\rangle = \underbrace{-\rho\langle\tilde{u}\tilde{w}\rangle}_{\langle\tau_f\rangle} \underbrace{-\rho\langle\overline{u'w'}\rangle}_{\langle\tau_{uw}\rangle} \underbrace{+\rho\upsilon\frac{\mathrm{d}\langle\bar{u}\rangle}{\mathrm{d}z}}_{\langle\tau_{vis}\rangle} + \int_z^h (f_v + f_p)\,\mathrm{d}z, \tag{2.6}$$

where $\langle\tau_f\rangle$ is the form-induced shear stress (FISS) or dispersive stress (that is, $-\rho\langle\tilde{u}\tilde{w}\rangle$), $\langle\tau_{uw}\rangle$ is the DA Reynolds shear stress (RSS) (that is, $-\rho\langle\overline{u'w'}\rangle$), $\langle\tau_{vis}\rangle$ is the DA viscous shear stress (VSS) (that is, $\rho\upsilon(\mathrm{d}\langle\bar{u}\rangle/\mathrm{d}z)$), h is the flow depth, and f_v and f_p are the drag forces induced by viscous and pressure forces, respectively, below the roughness crest ($z < 0$). The momentum balance in the main flow produces $\langle\bar{\tau}\rangle = \langle\tau_f\rangle + \langle\tau_{uw}\rangle + \langle\tau_{vis}\rangle$. Importantly, below the crest, the total drag effects are counted in the total shear stress $\langle\bar{\tau}\rangle$ computation.

3. Numerical experiments and bed configuration

To investigate the influence of permeability on the turbulence characteristics over a rough bed, three sets of bed configurations were considered, as shown in figure 2, and the hydraulic parameters are listed in table 1. Case H involved open-channel flow over closely packed hemispheres forming the bed, which was considered as rough and impermeable. On the other hand, cases S and L were made of three closely packed layers of spheres with the same diameters d as the hemispheres of case H, and the packed spheres were considered as rough and permeable beds. The bed thickness H was $0.5d$ for the impermeable bed and $3d$ for permeable beds. To avoid an influence of the impermeable wall at $z = -H$ below the porous medium on the free flow, it was required that H should be much larger than the penetration depth of turbulence inside the permeable wall. We changed the bottom boundary condition from a solid boundary to a symmetry boundary for case L2. Results showed that the first and second statistics were only influenced near the bottom. In addition, case L2 created a pore space of straight tubes. Similar porous media were adopted in many experiments

https://doi.org/10.1017/jfm.2018.314 Published online by Cambridge University Press

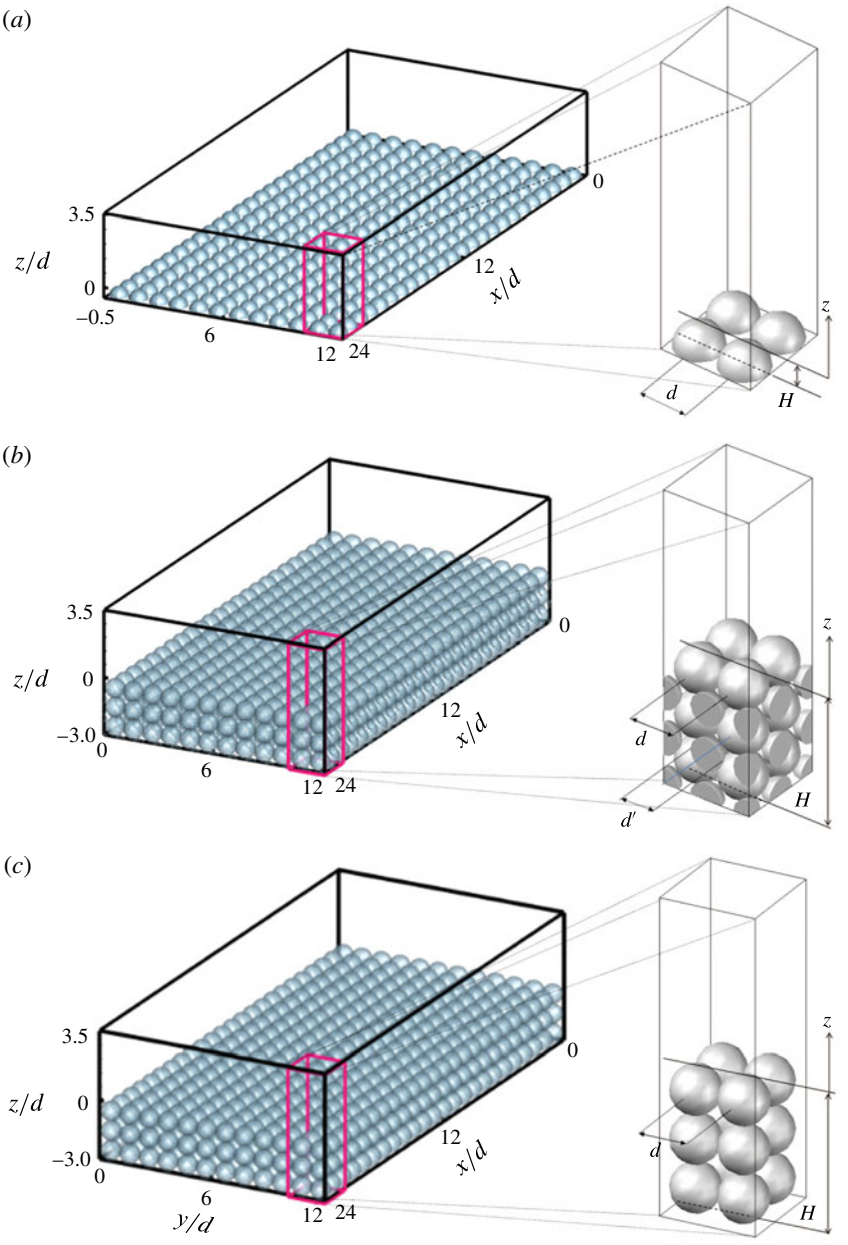

FIGURE 2. (Colour online) Computational geometry of impermeable and permeable beds: (*a*) hemisphere packing (case H), representing rough and impermeable beds; (*b*) small sphere packing (case S), representing rough and moderately permeable beds; and (*c*) large sphere packing (case L), representing rough and highly permeable beds.

(Dybbs & Edwards 1984; Horton & Pokrajac 2009; Manes *et al.* 2009) and simulations (Liu & Prosperetti 2011; Chaitanya & Sourabh 2016; Kuwata & Suga 2016). The cross-section of the pores varied between a $d \times d$ square and a diamond-shaped throat with a minimum pore diameter of $0.41d$. The cross-section and the longitudinal

https://doi.org/10.1017/jfm.2018.314 Published online by Cambridge University Press

section of the total simulated bed comprised of 39 pores and 75 pores, respectively, which can be regarded as a representative porous medium comprising $O(10)$ pores. The main difference between cases S and L is that, in case S, another kind of smaller spheres with diameter $d'(=0.73d)$ was introduced into the interspace of spheres, which led to a greater number of pores and a lower bed permeability than case L. Hence, cases S and L allowed the surface flow to interact with the interfacial fluid within the bed. Since the three bed configurations were characterized by identical surface roughness, the comparison of surface flow velocity statistics allowed the effects of permeability to be distinguished (Manes *et al.* 2009).

The scales of flow field for three bed configurations were considered to be the same. The flow depth h was set as $3.5d$, which is defined as the vertical distance from the crest of the roughness elements to the free surface. The flow depth condition with respect to the sphere diameter was the same as that of Manes *et al.* (2009) and close to that of Dey & Das (2012), who considered the flow depth as 4.2 times the median diameter of gravels. The computational domain of the main flow region spanned $6.8h \times 3.4h \times h$ (figure 2*a*). The size was slightly larger than $2\pi h \times \pi h \times h$, as is commonly accepted to include all relevant turbulence structures (Bomminayuni & Stoesser 2011). Cyclic boundary conditions were used in the streamwise and spanwise directions. The free surface was set as a frictionless rigid lid and treated as a plane of symmetry. The hydraulic parameters of the three bed configurations are provided in table 1.

The permeability Reynolds number ($Re_K = K^{0.5}u_*/\upsilon$, where K is the permeability of the bed, $u_* = (\tau/\rho)^{0.5}$ is the shear velocity, $\tau = h\,\mathrm{d}p/\mathrm{d}x$ and $\mathrm{d}p/\mathrm{d}x$ is the pressure gradient driving the flow) unifies two classical flow typologies, namely impermeable boundary-layer flow ($Re_K \ll 1$) and highly permeable canopy flow ($Re_K \gg 1$) (Breugem *et al.* 2006; Voermans, Ghisalberti & Ivey 2017). In aquatic systems, Re_K typically lies in the range 0.01–10 (Rosgen 1994; Wilson, Huettel & Klein 2008). As shown in table 1, the LES was carried out at different bulk Reynolds numbers Re_b ($= hU_b/\upsilon$, where U_b is the bulk velocity). By varying the bulk Reynolds number Re_b, one kind of bed configuration allowed a large simulated range of Re_K. The computation was run for 150 dimensionless time units (h/U_b), which was approximately 22 flow-through times, to obtain a fully developed turbulent flow (one flow-through time is the length of one flow field divided by the mean velocity U_b; here it was $6.8h/U_b$). The calculation was run for another 400 dimensional time units (h/U_b), i.e. approximately 58 flow-through times, during which the data for the statistics were sampled. The flow velocity in the vicinity of the inlet from $-0.5d$ to $3.5d$ was set as unity for impermeable beds and from $-3d$ to $3.5d$ for permeable beds. The velocity profile was developed automatically once the model was run. The code was parallelized using the message-passing interface and the domain-decomposition technique. For all cases, the computational area was divided into 72 domains in the horizontal direction, i.e. 12 domains in the x direction and six domains in the y direction. Every domain contained 2×2 spheres in the xy-plane. The uniform spacing of the grids was Δ^{x+}, $\Delta^{y+} = (\Delta^x, \Delta^y) \times u_*/\upsilon$. In the vertical (wall-normal) direction, the grids were refined near the interface between the fluid and the first sphere with a minimum value, and at the free surface with a maximum value. The per repeating domain and grid sizes are listed in table 1. In the following parts, we mainly use case H, case S3 and case L2 to show and discuss the effects of bed permeability on the first-, second- and third-order flow statistics and flow visualizations, as they are typical permeable beds with the same $Re_b = 15\,000$ and different $Re_K = 0$, 2.7 and 27.4, respectively. Then, all cases over permeable beds are considered to parametrize some flow quantities with Re_K.

https://doi.org/10.1017/jfm.2018.314 Published online by Cambridge University Press

Case	d_p/d	d^+	h^+	ε_c	Re_b	Re_K	Grid size $N_x \times N_y \times N_z$	Grid spacing Δ^{z+}
H	0.5	281.9	986.8	0	15 000	0	$42 \times 42 \times 84$	1.58–17.44
S1	0.9	246.3	861.9	0.166	4 000	0.7	$42 \times 42 \times 132$	0.85–9.55
S2	0.9	476.4	1667.4	0.166	8 000	1.4	$42 \times 42 \times 132$	1.65–18.47
S3	0.9	929.0	3251.5	0.166	15 000	2.7	$42 \times 42 \times 132$	3.26–36.00
S4	0.9	1455.2	5093.1	0.166	30 000	5.7	$54 \times 54 \times 166$	5.35–54.73
S5	0.9	2444.7	8556.5	0.166	50 000	10.3	$54 \times 54 \times 166$	8.87–89.55
L1	1	514.6	1801.1	0.476	8 000	12.7	$42 \times 42 \times 132$	1.80–19.85
L2	1	1113.8	3898.3	0.476	15 000	27.4	$42 \times 42 \times 132$	3.89–42.96
L3	1	2907.0	10174.6	0.476	50 000	109	$54 \times 54 \times 166$	10.40–96.06

TABLE 1. Hydraulic parameters and computational geometry for simulations.

Note: In the above, d is the diameter of hemispheres for the impermeable bed and large spheres for permeable beds, $d_p = 6V_p/A_p$ (that is, the mean particle diameter in terms of volume V_p and surface area A_p of the solid obstacles), ε_c is the porosity, Re_K is the permeability Reynolds number, $Re_K = K^{0.5}u_*/\upsilon$; $K = d_p^2\varepsilon_c^3(1-\varepsilon_c)^{-2}/180$, that is, the permeability of the bed (Breugem *et al.* 2006), u_* is the shear velocity and N_x, N_y and N_z are the grid node numbers of per repeating domain in the x, y and z directions, respectively. The resolution is per repeating unit.

To test for grid convergence for turbulence statistics, we compare the LES of three configurations with progressively refined grids to assess the effects of grid size, including a coarse mesh, a medium mesh and a fine mesh for every case. All cases were carried out with $Re_b = 15\,000$. The details of mesh are provided in table 2. The first and second-order DA statistics are compared in figure 3. The results show a similar tendency for the three cases. As shown in figure 3(*a*,*c*,*e*), the first-order statistics are insensitive to the grid resolution in the medium grid and fine grid simulation, while a slight overestimate in velocity gradient is found near the bed in the coarse grid simulation. The second-order statistics are also insensitive to grid size when the grids reach the medium size, as shown in figure 3(*b*,*d*,*f*). The larger grid sizes adopted in the coarse grid simulation lead to an overestimate in Reynolds normal stress through the entire flow depth, especially near the flow surface, as a maximum grid size is adopted there. Overall, the results confirm that a further refined mesh resolution would not lead to discrepancies in the first- and second-order flow statistics when the grid size reaches a medium size.

4. Results and discussion

4.1. *The double-averaged velocity*

A customary parameterization of the log law is

$$\langle\bar{u}\rangle^+ = \frac{1}{\kappa}\ln\left(\frac{z^+ + z_0^+}{k_s^+}\right), \tag{4.1}$$

where $\langle\bar{u}\rangle^+ = \langle\bar{u}\rangle/u_*$, $\langle\bar{u}\rangle$ is the DA streamwise velocity, u_* is the shear velocity, $z^+ = zu_*/\upsilon$, z is the vertical distance from the crest of the roughness elements, $z_0^+ = z_0u_*/\upsilon$, z_0 is the zero-displacement height, $k_s^+ = k_su_*/\upsilon$, k_s is the equivalent roughness height and κ is equivalent to the von Kármán constant. To plot the data $\langle\bar{u}\rangle^+$ as a function

https://doi.org/10.1017/jfm.2018.314 Published online by Cambridge University Press

Case	Grid	Grid size $N_x \times N_y \times N_z$	Grid spacing in wall units Δ^{x+}	Δ^{y+}	Δ^{z+}
Case H	Fine	$54 \times 54 \times 106$	6.52	6.52	1.43–11.95
	Medium	$42 \times 42 \times 84$	8.39	8.39	1.58–17.44
	Coarse	$34 \times 34 \times 68$	10.36	10.36	2.23–23.90
Case S3	Fine	$54 \times 54 \times 166$	13.47	13.47	2.61–26.67
	Medium	$42 \times 42 \times 132$	17.32	17.32	3.26–36.00
	Coarse	$34 \times 34 \times 106$	21.39	21.39	4.13–52.78
Case L2	Fine	$54 \times 54 \times 166$	16.08	16.08	3.11–31.82
	Medium	$42 \times 42 \times 132$	20.67	20.67	3.89–42.96
	Coarse	$34 \times 34 \times 106$	25.53	25.53	4.93–62.98

TABLE 2. Grid parameters of the large-eddy simulation on different grids.

Note: In the above, N_x, N_y and N_z are the grid node number in x, y and z directions, respectively.

of dimensionless vertical distance $z^+ + z_0^+$ for the three cases, a prior estimation of z_0^+ is required. Subsequent determination of κ and k_s^+ is also essential to fit the data to the log law. The determination of the parameters was done independently, as follows: the data set for $\langle\bar{u}\rangle^+ = \langle\bar{u}\rangle/u_*$ corresponding to $z^+ + z_0^+$ was prepared for the analysis. Assuming a very small trial value of z_0^+, the values of κ and z_0 were determined from (4.1) using the regression analysis, and the regression coefficient (RC) was obtained. Then, z_0^+ was incrementally increased by a small value, and κ and k_s^+ were determined in the same way, until RC reached the maximum. The corresponding values of z_0^+, κ and k_s^+ were then determined as $z_0^+ = 120.4$, 422.7 and 974.5, $\kappa = 0.41$, 0.34 and 0.32, and $k_s^+ = 10.6$, 107.8 and 295.2 for cases H, S3 and L2, respectively. Figure 4 shows the dimensionless DA streamwise velocity $\langle\bar{u}\rangle^+$ as a function of dimensionless vertical distance $z^+ + z_0^+$ for cases H, S3 and L2. Three cases are plotted along with the results of Defina (1996) and Singh *et al.* (2007) corresponding to k_s^+ values of 3.4 and 9.6. Earlier studies revealed that the downshift of the time-averaged velocity profile increases with an increase in k_s^+ $(= k_s u_*/\upsilon)$. The $\langle\bar{u}\rangle^+$-profiles obtained from the LES exhibit a similar trend, confirming the legitimacy of the findings. An increasing trend of z_0^+ with Re_K was also obtained by Suga *et al.* (2010), which is in conformity with the results obtained from this study. In addition, an inflection point in the $\langle\bar{u}\rangle^+$-profiles appears at the crest of the roughness elements for these three cases, resulting from a strong flow separation from the crest of the hemispherical or spherical topography (Castro, Cheng & Reynolds 2006; Coceal *et al.* 2007). Above the crest, it is apparent that the $\langle\bar{u}\rangle^+$-profiles preserve the log law, and the logarithmic layer is approximately $z^+ \in [54 : 780]$ for case H, $z^+ \in [80 : 1400]$ for case S3 and $z^+ \in [115 : 1950]$ for case L2. Nezu (2005) and Suga *et al.* (2010) observed that κ decreases with an increase in permeability Reynolds number Re_K, which is also found in the simulated results. On the other hand, below the crest, the $\langle\bar{u}\rangle^+$-profiles follow a polynomial function having the form $\langle\bar{u}\rangle^+ = a + bz^+ + cz^{+2} + dz^{+3}$ in these three cases, where a, b, c and d are the coefficients. It is in conformity with the results obtained by Sarkar & Dey (2010), Dey & Das (2012) and Sarkar *et al.* (2016).

https://doi.org/10.1017/jfm.2018.314 Published online by Cambridge University Press

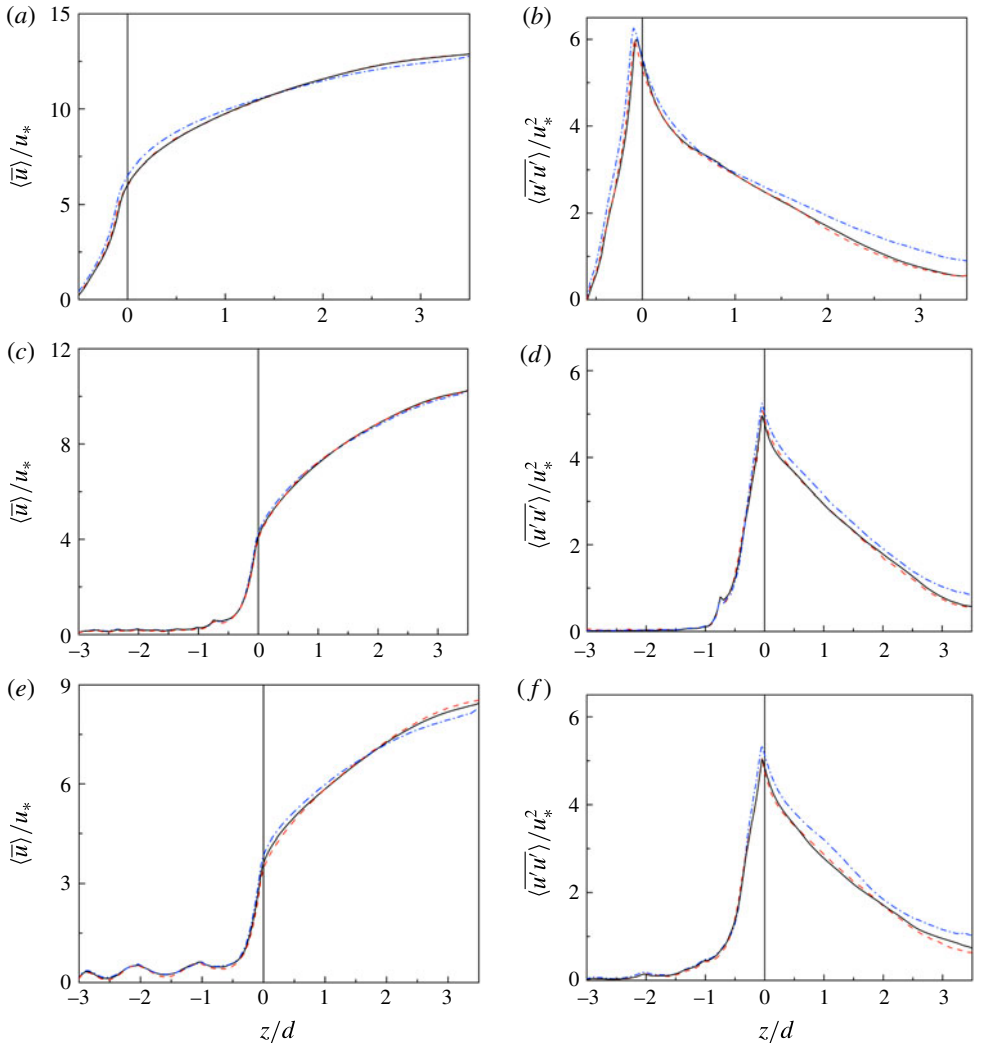

FIGURE 3. (Colour online) Grid convergence test at $Re_b = 15\,000$. (*a*,*c*,*e*) are DA velocity profiles normalized by u_* for case H, case S3 and case L2, respectively. (*b*,*d*,*f*) are DA streamwise normal stress profiles normalized by u_*^2 for case H, case S3 and case L2, respectively. The red dashed, black solid and blue dashed-dotted lines represent the fine, medium and coarse grids, respectively.

4.2. *The double-averaged Reynolds normal stresses*

Figure 5(*a–c*) presents the dimensionless DA streamwise, spanwise and vertical Reynolds normal stresses, $(\langle\overline{u'u'}\rangle, \langle\overline{v'v'}\rangle, \langle\overline{w'w'}\rangle) \times u_*^{-2}$, as a function of dimensionless vertical distance z/d for cases H, S3 and L2. An additional simulation with the same bulk Reynolds number $Re_b = 15\,000$ was carried out for the flow over an impermeable smooth bed, which was characterized by a coarser grid in the horizontal ($\Delta^{x+} = \Delta^{y+} \approx 16$) than case H but which is finer near the smooth wall with $\Delta^{z+} \approx 1$. The data for the streamwise and vertical Reynolds normal stresses obtained experimentally by Manes *et al.* (2009) are also plotted along with the simulated results.

https://doi.org/10.1017/jfm.2018.314 Published online by Cambridge University Press

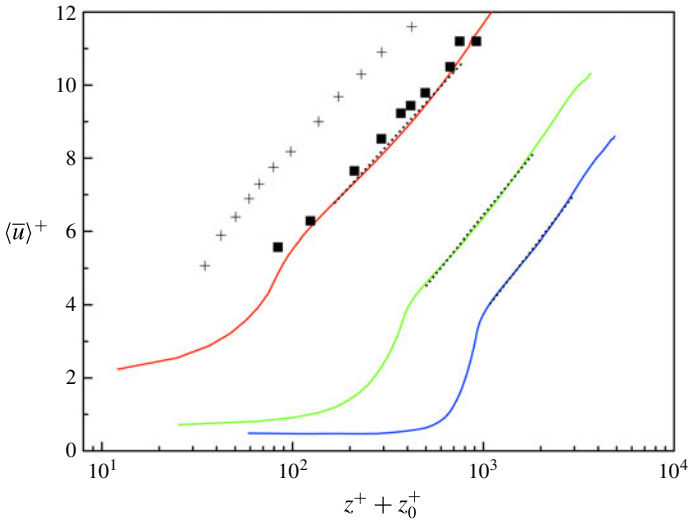

FIGURE 4. (Colour online) Vertical profiles of DA streamwise velocity for cases H (red solid line refers to $k_s^+ = 10.6$), S3 (green solid line refers to $k_s^+ = 107.8$) and L2 (blue solid line refers to $k_s^+ = 295.2$). Symbol + represents the DNS results with a layer of spheres reported by Singh, Sandham & Williams (2007) for $k_s^+ = 3.4$, solid square symbol represents the experimental data for the flow over a rough bed reported by Defina (1996) for $k_s^+ = 9.6$ and dotted lines represent the log-law profile for each case.

The bed was covered with five-layer spheres in a cubic pattern in those experiments, which is similar to case L2. As shown in figure 5(*a*,*c*), the experimental data plots are in satisfactory agreement with the simulated results of case L2 over the crest. However, below the crest, the profiles of simulated DA streamwise and vertical Reynolds normal stress depart from those of Manes *et al.* (2009), especially for the simulated vertical Reynolds stress values, which are approximately 1.5 times the experimental values. The disagreement is attributed to the different DA procedures. Due to the experimental limitation, the laser light sheet in PIV was placed at two streamwise-oriented vertical planes: one over the top of the spheres and another over their valleys. The spatially averaged portions in the spanwise direction only include these two sections. In this study, we use the total area at an elevation z. If we had adopted the same DA procedure as that adopted by Manes *et al.* (2009), we could have got the solid lines shown in figure 5(*a*,*c*), which show a better agreement with the experimental data. It illustrates that the statistics including two sections (top and valley) may underestimate the DA Reynolds normal stress, resulting from the lack of sampling volume in the spanwise direction. In addition, the DA Reynolds normal stresses diminish rapidly inside the permeable wall, becoming negligible below $z/d = -2$. This indicates that the turbulent flow in the open channel is not influenced by the presence of the solid wall at $z/d = -3$.

In figure 5(*a*), the simulated profiles of DA streamwise Reynolds normal stress for rough beds, i.e. case H, case S3 and case L2, collapse on that for impermeable smooth beds for $z/d > 1.5$, substantiating the wall similarity hypothesis (Townsend 1976). In contrast, the profiles of the DA spanwise and vertical normal stresses exhibit less similarity. Breugem *et al.* (2006) also observed that the DA streamwise Reynolds normal stress preserves similarity in the outer region over a permeable bed, while

https://doi.org/10.1017/jfm.2018.314 Published online by Cambridge University Press

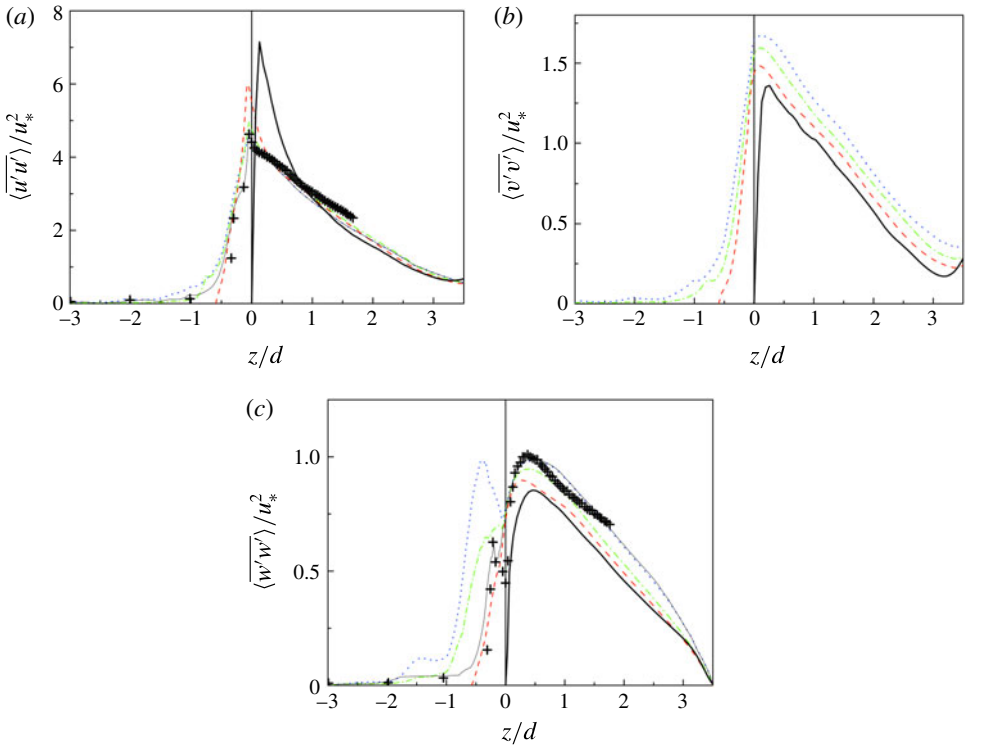

FIGURE 5. (Colour online) Simulated results of (*a*) DA streamwise Reynolds normal stress, (*b*) DA spanwise Reynolds normal stress and (*c*) DA vertical Reynolds normal stress for case H (red dashed line), case S3 (green dashed-dotted line) and case L2 (blue dotted line). Symbol + represents the experimental data with five layers of spheres reported by Manes *et al.* (2009). The thin solid line represents the results of case L2, which were double-averaged by a procedure similar to that of Manes *et al.* (2009). The thick solid line represents the results of the flow over an impermeable smooth bed with the same bulk Reynolds number $Re_b = 15\,000$.

the similarity disappeared in the spanwise and vertical Reynolds normal stresses. Furthermore, Krogstad & Antonia (1999) measured boundary-layer flows over rough walls. They reported that the vertical Reynolds normal stress increases significantly and the streamwise Reynolds normal stress remains unchanged as compared to a smooth wall. However, Manes *et al.* (2009) observed that the vertical Reynolds normal stress shows no obvious difference between permeable and impermeable beds over the crest. The reason is attributed to the fact that they used one layer of spheres to represent the impermeable bed and the deep cavities between the spheres to cause larger fluctuations over the bed than for the hemispheres used in this study.

Around the crest, the peaks in the DA streamwise Reynolds stress are lower for the case with higher bed permeability, whereas the peaks are higher for the case with higher bed permeability in the spanwise and vertical Reynolds stresses, which is attributed to the weakening effects of wall-blocking in permeable beds.

Below the crest (within the interfacial layer), the streamwise and spanwise Reynolds normal stresses show much smaller differences among the cases than the vertical Reynolds normal stress, which exhibits fluctuations near $z/d \approx -0.34$ for

https://doi.org/10.1017/jfm.2018.314 Published online by Cambridge University Press

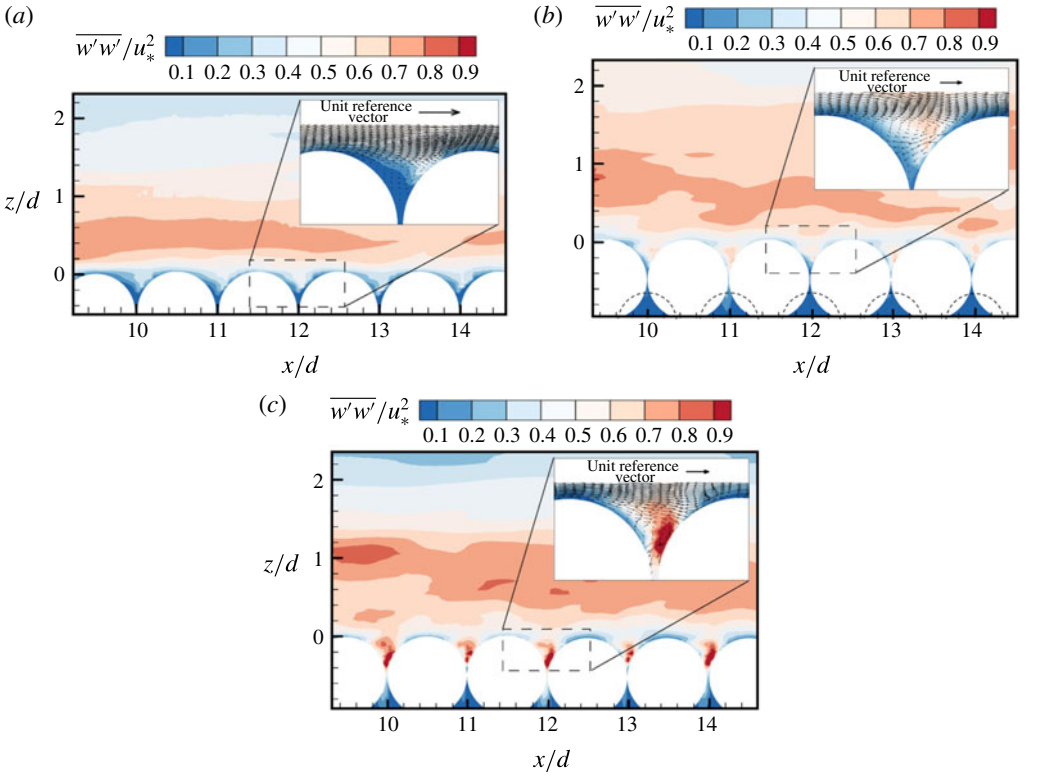

FIGURE 6. (Colour online) Contours of vertical Reynolds normal stresses and the time-averaged velocity vectors on the xz-plane at $y/d = 6.5$ through the centres of hemispheres for (a) case H and large spheres for (b) case S3 and (c) case L2. The dotted line in case S3 shows the periphery of small spheres ($d' = 0.73d$).

permeable beds. Interestingly, in case L2, the peaks of the vertical Reynolds normal stresses at $z/d \approx -0.34$ (within the interfacial layer) and $z/d \approx 0.47$ (above the crest) are comparable, illustrating a more pronounced weakening effect of the wall-blocking within the interfacial layer. This weakening effect can be clearly found in figure 6, where the contours of the vertical Reynolds normal stress are shown on the xz-plane at $y/d = 6.5$ through the centres of the hemispheres for case H and the large spheres for cases S3 and L2. Above the crests of the spheres, the vertical Reynolds normal stress vanishes rapidly for the three cases, while within the valley formed by the spheres, the fluctuations exhibit different trends. From the time-averaged velocity vectors shown in the insets to figure 6, it is apparent that the vortices shed from the crests of the upstream sphere due to flow separation and then the fluid infiltrate through the interstices of the spheres forming the valleys. As a result of increasing the bed permeability from case S3 to case L2, the shedding gets deeper and causes a more intense vertical Reynolds normal stress. On the other hand, as a result of wall-blocking effects in case H, the vortex shedding is prevented from infiltrating into the bed formed by the hemispheres, leading to a more obvious recirculatory flow within the valley, which decreases the vertical Reynolds normal stress.

The locations which were selected in the line- and point-averaging procedures are shown in figure 7. It is noticeable that the section in xz-plane adopted in figure 6

https://doi.org/10.1017/jfm.2018.314 Published online by Cambridge University Press

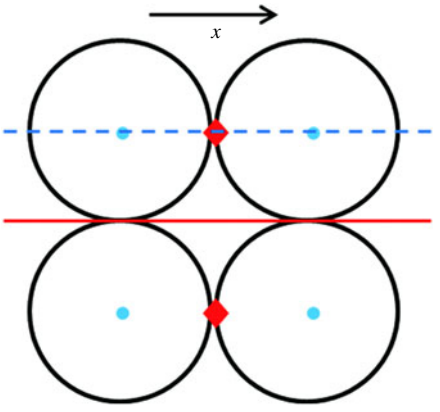

FIGURE 7. (Colour online) Top view of a repeating domain to illustrate the different averaging locations. The red solid line lies over the valley and the blue dashed line lies over the top. The red diamond symbols indicate the valley points and the blue circles the top points.

corresponds to the line over the crest in figure 7. The difference in vertical Reynolds normal stresses between the flow zones near the crests and within the valleys is further exhibited in figure 8. It demonstrates the time- and line-averaged vertical profiles for the wall-normal Reynolds stress in the streamwise direction for each crest and valley side. In addition, the point-averaged vertical profiles are also shown in figure 9.

Above the bed, figure 8(*a*) shows that the line-averaged Reynolds stress $\langle\overline{w'w'}\rangle_l/u_*^2$ for the top side reaches a higher peak than those for the valley side, which is caused by a strong shear layer shedding from the crest. Below the bed, $\langle\overline{w'w'}\rangle_l/u_*^2$ over the top side decreases more rapidly to zero than that over the valley side, due to the limited space between spheres. However, for permeable beds (i.e. case S3 and case L2) shown in figure 8(*b*,*c*), the peaks of $\langle\overline{w'w'}\rangle_l/u_*^2$ over the valley side are higher than those over the top side. The reason is attributed to the fact that as beds become more permeable, the momentum transfer across the bed increases. The wall-blocking effects over the valley side are apparently less than those over the top side. It causes a slightly higher peak of $\langle\overline{w'w'}\rangle_l/u_*^2$ for the valley side above the bed. Vertical Reynolds normal stresses for the valley side are also compared among three cases. As shown in figure 8(*d*), above the crest ($z/d > 0$), the vertical Reynolds normal stresses are higher for the case with higher bed permeability. Below the crest, there exists another peak for permeable beds, especially for case L2. Similar tendencies are also observed in the point-averaged results, as shown in figure 9. Further, the valley points are close to spheres below the crest, while the valley line includes some points located in the diamond-shaped pore space (from the top view, as shown in figure 7), so the increase in the peak value is lower in the valley line-averaged results than the valley point-averaged results, and the corresponding elevations z/d are -0.5 and -0.2, respectively.

4.3. *The form-induced normal stresses*

Figure 10(*a–c*) depicts the dimensionless streamwise, spanwise and vertical form-induced normal stresses, $(\langle\tilde{u}\tilde{u}\rangle, \langle\tilde{v}\tilde{v}\rangle, \langle\tilde{w}\tilde{w}\rangle) \times u_*^{-2}$, as a function of dimensionless vertical distance z/d for cases H, S3 and L2. Having compared the results in

https://doi.org/10.1017/jfm.2018.314 Published online by Cambridge University Press

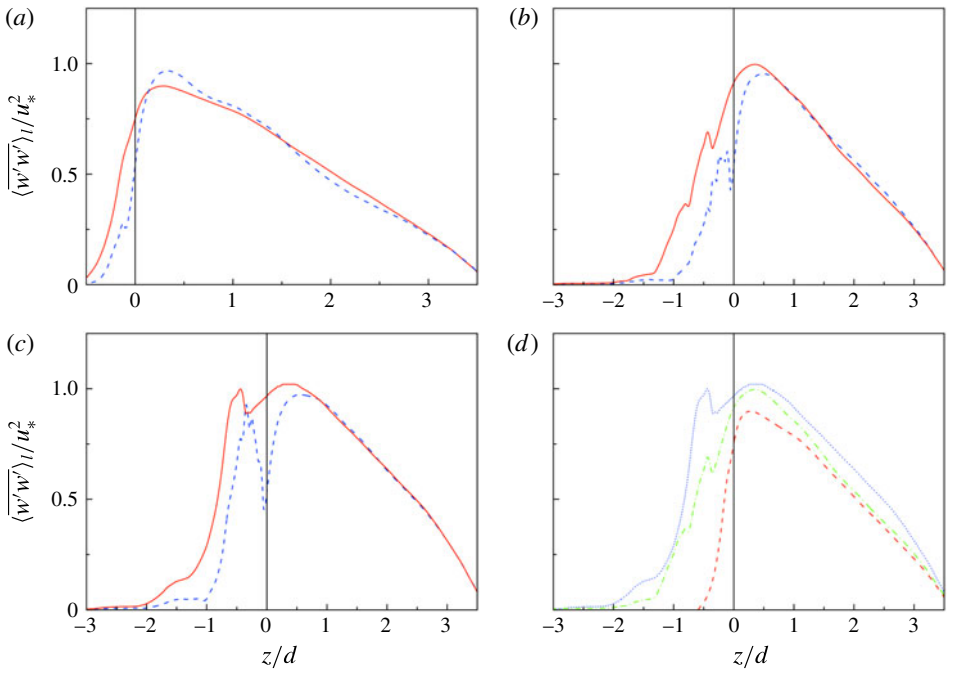

FIGURE 8. (Colour online) Time- and line-averaged vertical profiles of vertical Reynolds normal stresses for (*a*) case H, (*b*) case S3 and (*c*) case L2. For (*a*,*b*,*c*), the red solid line corresponds to the valley and the blue dashed line to the top. For (*d*), the red dashed line refers to case H, the green dashed-dotted line to case S3 and the blue dotted line to case L2.

figures 5 and 10, it is evident that the vertical and spanwise form-induced normal stresses are smaller than the corresponding components of the Reynolds normal stresses. This is consistent with previous experimental studies of a rough wall and canopy (Nikora *et al.* 2001; Mignot *et al.* 2009*a*)). On the other hand, the streamwise form-induced normal stress is comparable to the streamwise Reynolds normal stress, which is characterized by the relatively low submergence (Pokrajac *et al.* 2007). Within the interfacial layer near $z/d = -0.4$, the form-induced normal stresses become maximum, exhibiting peaks in their profiles for the three cases. In the $\langle\tilde{u}\tilde{u}\rangle$-profiles, the peak value of case H (with impermeable bed) is larger than other two cases (with permeable beds), while the peak values in $\langle\tilde{v}\tilde{v}\rangle$- and $\langle\tilde{w}\tilde{w}\rangle$-profiles increase with permeability. It can be argued from figure 6 that vortex shedding and recirculation within the valley formed by the spheres cause the spatial fluctuations of velocity for the three cases, leading to peaks near $z/d = -0.4$. Moreover, the effects of the wall-blocking result in a more stable recirculation in the streamwise direction, causing a relative high magnitude of streamwise form-induced normal stress in case H. However, the vertical and spanwise form-induced normal stresses are enhanced with an increase in permeability. The reason is attributed to the more intense spatial fluctuations of time-averaged flow in those two directions below the crest. In case H (with impermeable bed), the form-induced normal stresses are greater in the near-bed flow zone, where the time-averaged flow is directly influenced by the roughness elements, and they become negligible in the main flow. In contrast, in cases S3 and L2 (with permeable beds), the form-induced normal stresses remain finite even in

https://doi.org/10.1017/jfm.2018.314 Published online by Cambridge University Press

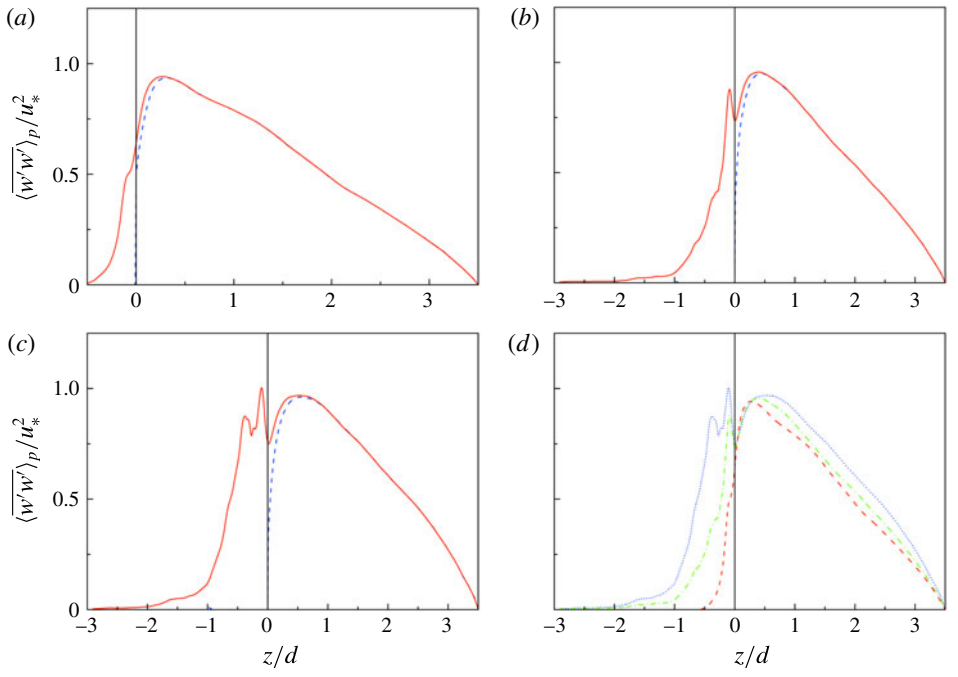

FIGURE 9. (Colour online) Time and point-averaged vertical profiles of vertical Reynolds normal stresses for (*a*) case H, (*b*) case S3 and (*c*) case L2. For (*a*,*b*,*c*), the red solid line corresponds to the valley and the blue dashed line to the top. For (*d*), the red dashed line refers to case H, the green dashed-dotted line to case S3 and the blue dotted line to case L2.

the main flow. This is triggered by secondary currents, which are discussed in the following section.

4.4. *Stress balance and turbulence structure*

Figure 11(*a*,*b*) shows the vertical profiles of the DA Reynolds shear stress $\langle \bar{\tau}_{uw} \rangle$ $(= -\rho \langle \overline{u'w'} \rangle)$ and stress balance for the three cases. All the stresses are made dimensionless by U_b^2, as the profiles of different cases can be separated and shown more clearly. Above the crest ($z > 0$), the total shear stress $\langle \bar{\tau} \rangle$ in (2.6) is balanced by the mean pressure gradient. It has a linear profile for $\langle \bar{\tau} \rangle (z > 0)/(\rho u_*^2) = 1 - z/h$ (Dey & Das 2012; Yuan & Piomelli 2014). As shown in figure 11(*a*), only for case H (with an impermeable bed) does the DA Reynolds shear stress follow the linear profile away from the roughness elements, while for cases S3 and L2, the shear stresses are damped near $z/d = 0.5$ and 1, respectively. Figure 11(*b*) shows that below the crest, since the time-averaged flow in the vicinity of the spheres is spatially heterogeneous, the form-induced shear stresses grow sharply with a decrease in z/d, attaining peaks at $z/d = -0.2$, -0.4 and -0.4 for cases H, S3 and L2, respectively, and then decrease with a further decrease in z/d. The trends of the form-induced shear stresses below the crest are consistent with the results obtained from the previous experimental and numerical studies on macro-rough walls (Mignot *et al.* 2009*a*; Yuan & Piomelli 2014). However, above the crest, only case H (with impermeable bed) follows the conventional trend that $-\langle \tilde{u}\tilde{w} \rangle$ decreases rapidly with an increase in elevation and is

https://doi.org/10.1017/jfm.2018.314 Published online by Cambridge University Press

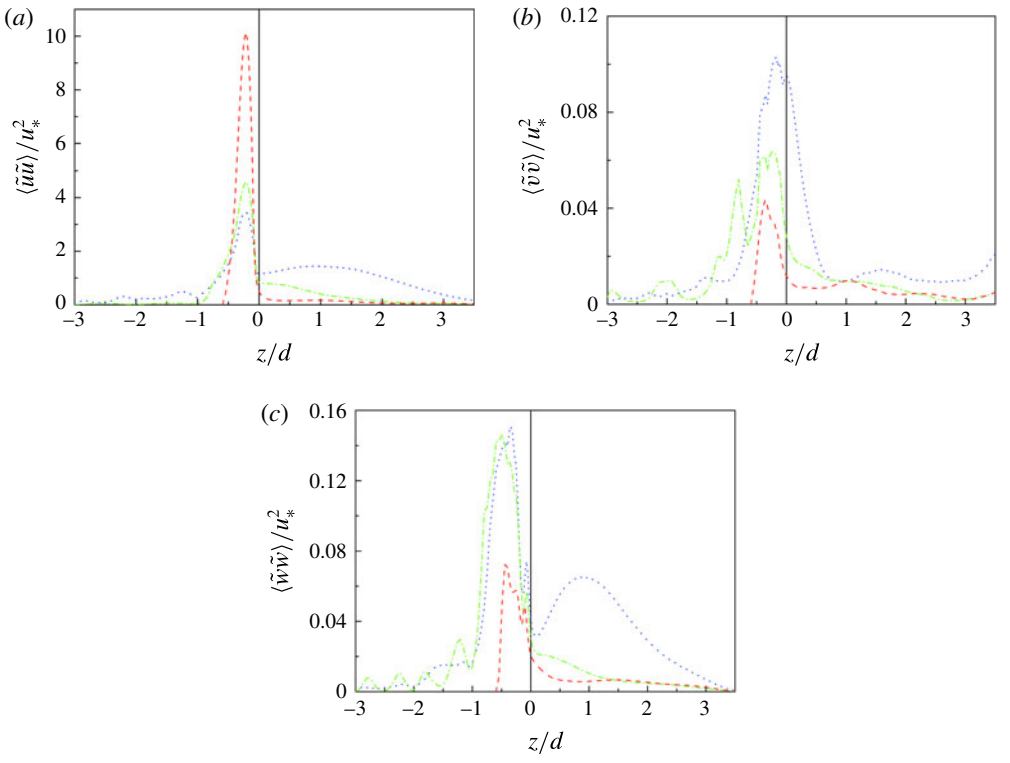

FIGURE 10. (Colour online) Simulated results of (*a*) streamwise form-induced normal stress, (*b*) spanwise form-induced normal stress and (*c*) vertical form-induced normal stress for case H (red dashed line), case S3 (green dashed-dotted line) and case L2 (blue dotted line).

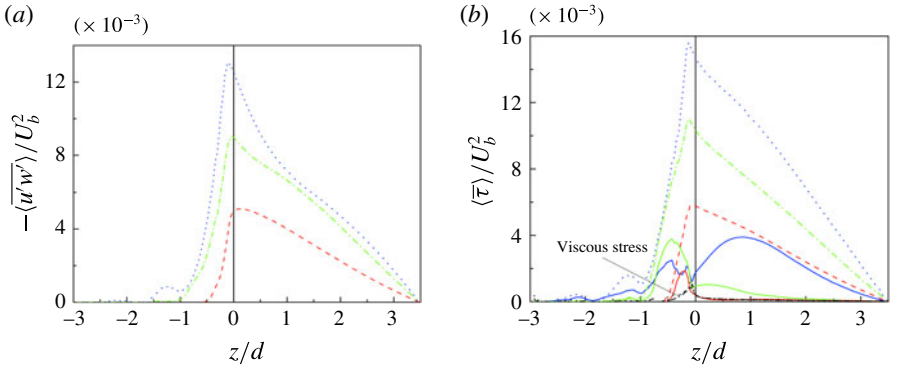

FIGURE 11. (Colour online) (*a*) DA Reynolds shear stress and (*b*) stress balance. Total shear stress for case H (red dashed line), case S3 (green dashed-dotted line) and case L2 (blue dotted line); form-induced shear stress for case H (red solid line), case S3 (green solid line) and case L2 (blue solid line). The viscous stresses for three cases are shown in black to distinguish them from the form-induced shear stresses.

https://doi.org/10.1017/jfm.2018.314 Published online by Cambridge University Press

negligible in the main flow. The form-induced shear stresses in cases S3 and L2 (with permeable beds) have their peaks near $z/d = 0.5$ and 1, respectively, and compensate for the damping of $-\langle\overline{u'w'}\rangle$, leading to linear profiles of the total shear stresses from zero at the free surface to a maximum near the crest (figure 11*b*). The form-induced shear stresses above the crest for permeable beds are induced by the time-averaged structure of secondary currents. Coleman *et al.* (2007) measured the velocity in planes parallel to the centreline over 2D transverse ribs and highlighted the role of secondary currents on momentum transfer. For the momentum balance along the streamwise line, they added the participating secondary current terms (namely, the integral from z to free surface h of $[\rho\langle\bar{v}\rangle\partial\langle\bar{u}\rangle/\partial y + \rho\langle\bar{w}\rangle\partial\langle\bar{u}\rangle/\partial z + \rho\partial\langle\overline{u'w'}\rangle/\partial y + \rho\partial\langle\tilde{u}\tilde{w}\rangle/\partial y]$) to (2.6). In this study, the roughness geometry and the flow geometry are periodic due to the sphere arrangement and the boundary conditions are cyclic in the streamwise and spanwise directions. To capture the large scale as well as the detailed flow structures, we adopted spatial averaging in a thin plane parallel to the mean bed, which included all points at an elevation, and so produced $\langle\bar{v}\rangle = \langle\bar{w}\rangle = 0$ and $\partial(\cdot)/\partial y = 0$. Then, the secondary current terms vanish and the effects of the secondary current are represented by the form-induced Reynolds shear stress $\langle\tau_f\rangle = -\rho\langle\tilde{u}\tilde{w}\rangle$. The contours of the time-averaged streamwise velocity $\bar{u}/U_b$ and the streamlines of the secondary currents $(\bar{v}, \bar{w})$ on the yz-plane at $x/d = 12.5$ through the centres of the hemispheres for case H and the large spheres for cases S3 and L2 are shown in figure 12(*a–c*). It is observed that for case H (with an impermeable bed), the spanwise distribution of $\bar{u}$ is nearly flat above the crest and there are small spanwise vortical flows at the junctions of the surface hemispheres. With an increase in permeability (cases S3 and L2), the spanwise fluctuations of $\bar{u}$ become more obvious and the size of the near-bed cells of the secondary currents increases to approximately $0.5d$–$3d$.

To investigate the spanwise turbulence structure in detail, the autocorrelation functions of streamwise and vertical velocity fluctuations, $\rho_{u'u'}$ and $\rho_{w'w'}$, are calculated at elevations of $z/d = 0$, 0.5, 1 and 1.5 respectively. They are expressed as

$$\rho_{u'u'}(\Delta y) = \frac{\displaystyle\int_0^{12d} u'(y)u'(y-\Delta y)\,\mathrm{d}y}{\displaystyle\int_0^{12d} u'^2(y)\,\mathrm{d}y}, \quad \rho_{w'w'}(\Delta y) = \frac{\displaystyle\int_0^{12d} w'(y)w'(y-\Delta y)\,\mathrm{d}y}{\displaystyle\int_0^{12d} w'^2(y)\,\mathrm{d}y}, \tag{4.2a,b}$$

where Δy is the spanwise spacing. Figure 13(*a–c*) presents the autocorrelation functions of the streamwise velocity fluctuations $\rho_{u'u'}(\Delta y/d)$ for cases H, S3 and L2, respectively. The direction of arrows indicates increasing elevation (i.e. $z/d = 0$, 0.5, 1 and 1.5). In essence, the increase in the spanwise spacing of the streamwise velocity fluctuations is characterized by relatively large secondary vortical structures, as was observed by Breugem *et al.* (2006) from the DNS study. Therefore, for each case, the increasing spanwise spacing with rising elevation illustrates that larger turbulent structures exist in the main flow compared with the near-bed flow zone. In case H, the autocorrelation $\rho_{u'u'}$ exhibits a local minimum spanwise spacing of $\Delta y/d \approx 0.5$ at $z/d = 0$. This local minimum value is associated with the average spanwise distance between low-speed and neighbouring high-speed fluid streaks (Breugem *et al.* 2006). The oscillations in $\rho_{u'u'}$-profiles indicate a periodic fluid streak in the spanwise direction. With an increase in permeability, the local minimum spanwise spacing at $z/d = 0$ increases from $\Delta y/d \approx 0.5$ (case H, with an impermeable bed) to $\Delta y/d \approx 3$ (case L2, with a highly permeable bed), being consistent with the size of the time-averaged secondary vortices in figure 12. Figure 13(*d–f*) shows the

https://doi.org/10.1017/jfm.2018.314 Published online by Cambridge University Press

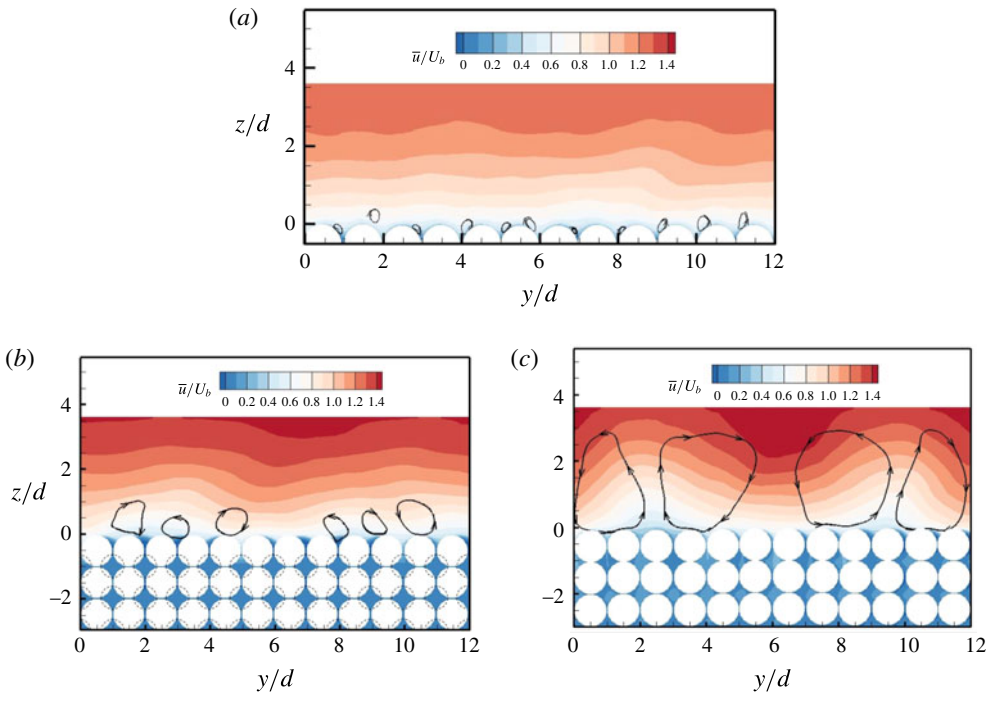

FIGURE 12. (Colour online) Contours of time-averaged streamwise velocity $\bar{u}/U_b$ and streamlines of the secondary currents $(\bar{v}, \bar{w})$ on the yz-plane at $x/d = 12.5$ through the centres of hemispheres for (a) case H and large spheres for (b) case S3 and (c) case L2. The dotted line in case S3 shows the periphery of small spheres $(d' = 0.73d)$.

autocorrelation functions of the vertical velocity fluctuations $\rho_{w'w'}(\Delta y/d)$ for cases H, S3 and L2, respectively. An increasing trend of spanwise spacing with an increase in bed permeability is also observed. Interestingly, with an increase in permeability, the autocorrelation function $\rho_{w'w'}$ is less dependent on elevation, indicating that the vertical classification of vortex scale decreases.

Figure 14$(a$–$c)$ shows the near-bed (at $z/d = 0.01$) contours of the dimensionless vorticity ω_z^+ $(= \omega_z \upsilon/U_b^2$, where $\omega_z = \partial v'/\partial x - \partial u'/\partial y)$ on the xy-plane for three cases. The elongated streaky structures, which result from the high- and low-speed fluid streaks and quasi-streamwise vortices, become shredded over the rough and impermeable wall. The longitudinal streamwise vortices become more twisted in case S3. On the other hand, in case L2, the streaky structures are not distinct, and some large-scale intermittent patches, which are considered to be caused by the KH type of instability, are apparent. In addition, strong vertical velocities are prevalent near the permeable bed surface because of the weakening effects of the wall-blocking. The vertical velocities also prevent the development of elongated streaky structures. To quantitatively analyse the statistics of the streamwise scaling, the pre-multiplied spectra at $z/d = 0.01$ are shown in figure 15. Spectra were computed as follows: first, the instantaneous spectra $E(k)$ were calculated for each instantaneous profile of velocity fluctuations using a fast Fourier transform technique. Second, all the spectra were averaged at each wavenumber k_x in order to decrease the confidence interval pertaining to each spectral estimate. It can be noticed that the spectra are presented in terms of the outer (h) scales. Figure 15(a) corresponds to the streamwise velocity.

https://doi.org/10.1017/jfm.2018.314 Published online by Cambridge University Press

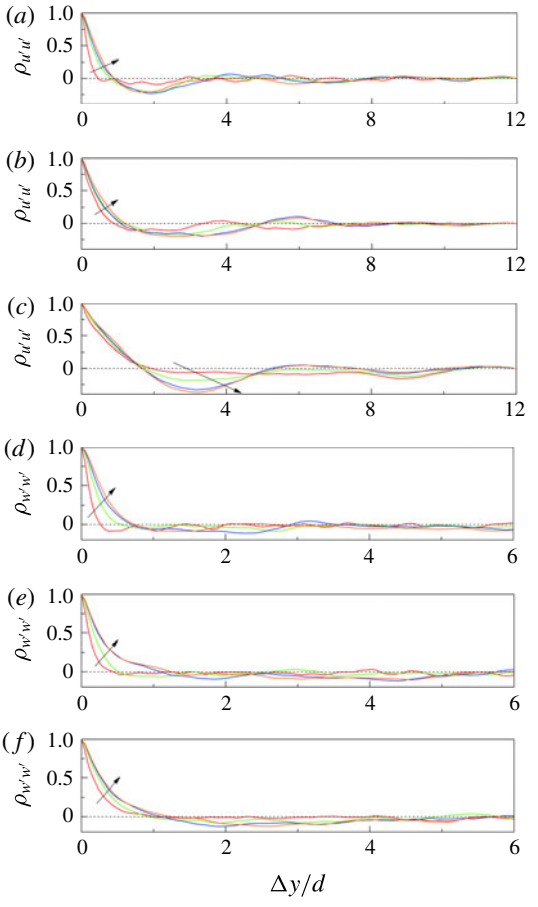

FIGURE 13. (Colour online) The autocorrelation functions of the streamwise velocity fluctuations $\rho_{u'u'}(\Delta y/d)$ for (*a*) case H, (*b*) case S3 and (*c*) case L2, and the autocorrelation functions of the vertical velocity fluctuations $\rho_{w'w'}(\Delta y/d)$ for (*d*) case H, (*e*) case S3 and (*f*) case L2. The group of curves in a case corresponds to different vertical elevations, increasing in the direction of the arrows as $z/d = 0$ (red line), 0.5 (green line), 1 (blue line) and 1.5 (orange line).

It shows that the spectra for case H in the range $5 < k_x h < 16$ are much higher than those for permeable beds. This means that coherent structures with lengths lying within 0.4–1.3h are more prevalent over the impermeable bed. For the wall-normal velocity in figure 15(*b*), the spectra are higher over permeable beds for $k_x h > 50$, corresponding to the enhanced wall-normal velocity fluctuations in the small-scale region ($< 0.1h$). Figure 15 also shows that for large-scale structures lying within $k_x h < 4$, the relative magnitudes are inverted as compared to the range $5 < k_x h < 16$. This is attributed to large-scale coherent structures on the valley side of the permeable beds. We use the isocontours of streamwise autocorrelations to explain this phenomenon.

The autocorrelation of the streamwise velocity is usually used to quantify the length of streaky structures (Kim, Moin & Moser 1987; Calmet & Magnaudet 1997; Breugem *et al.* 2006). For case H, the isocontours of the streamwise autocorrelation of the streamwise velocity and pressure are shown in figures 16 and 17, respectively.

https://doi.org/10.1017/jfm.2018.314 Published online by Cambridge University Press

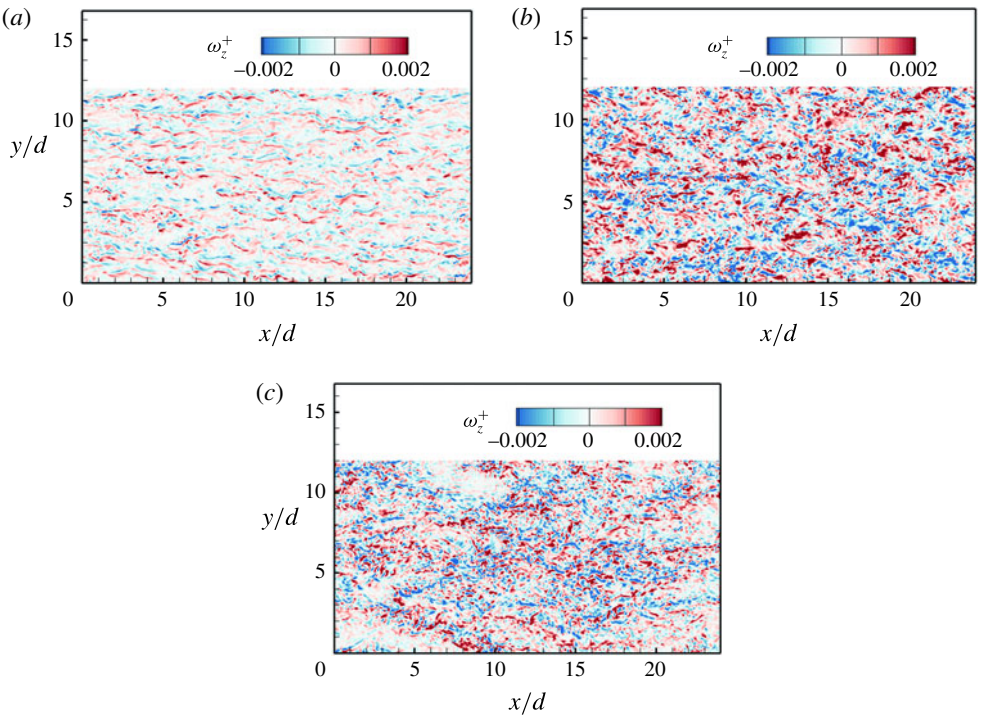

FIGURE 14. (Colour online) Contours of dimensionless vorticity ω_z^+ on the xy-plane at $z/d = 0.01$ for (a) case H, (b) case S3 and (c) case L2.

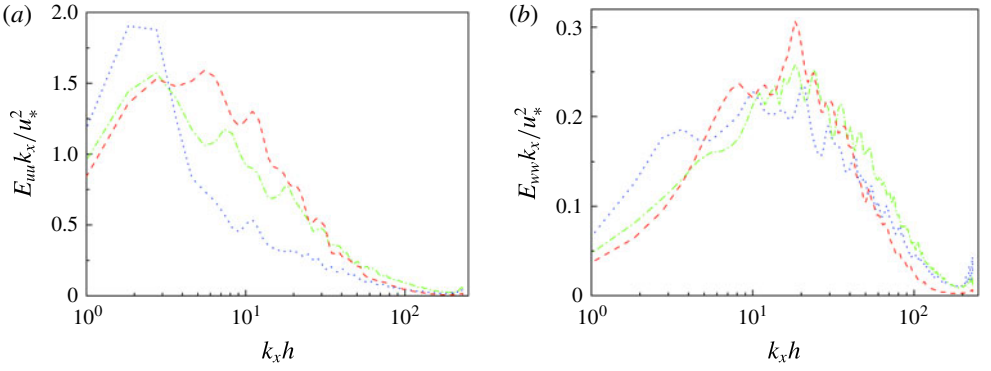

FIGURE 15. (Colour online) Pre-multiplied spectra calculated at $z/d = 0.01$: (a) streamwise velocity and (b) wall-normal velocity in case H (red dashed line), case S3 (green dashed-dotted line) and case L2 (blue dotted line).

It may be noted that this is a one-dimensional correlation, but plotted across the channel. As the bed is characterized by large roughness elements, which are regularly arranged, the spanwise heterogeneity was taken into account. Two typical streamwise planes are adopted, which correspond to the top and the valley. Within the top plane, figure 16(a) shows that the correlation distance is approximately $0.4h$ close to $z/h = 0$, which corresponds to a correlation distance of approximately 400 wall units.

https://doi.org/10.1017/jfm.2018.314 Published online by Cambridge University Press

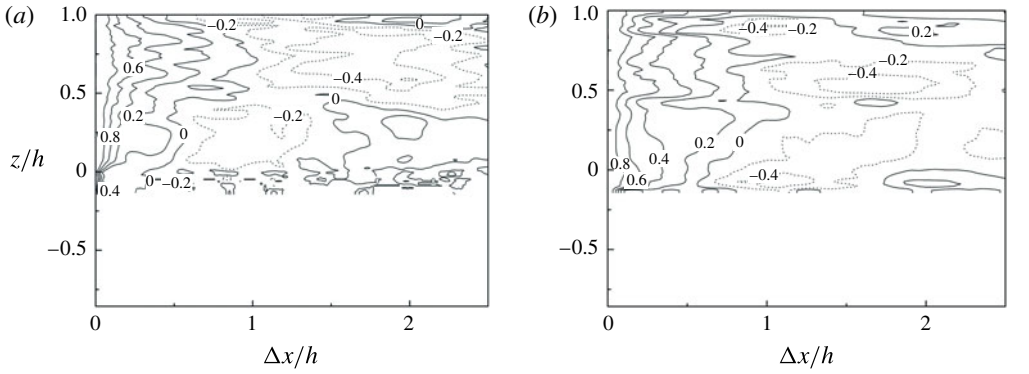

FIGURE 16. Isocontours of the autocorrelation of the streamwise velocity as a function of the streamwise spacing $\Delta x/h$, shown across the channel for case H. The solid and dashed lines correspond to positive and negative values, respectively. (*a*) A plane across the top of roughness (i.e. $y/d = 6.5$). (*b*) A plane across the valley of roughness (i.e. $y/d = 6$).

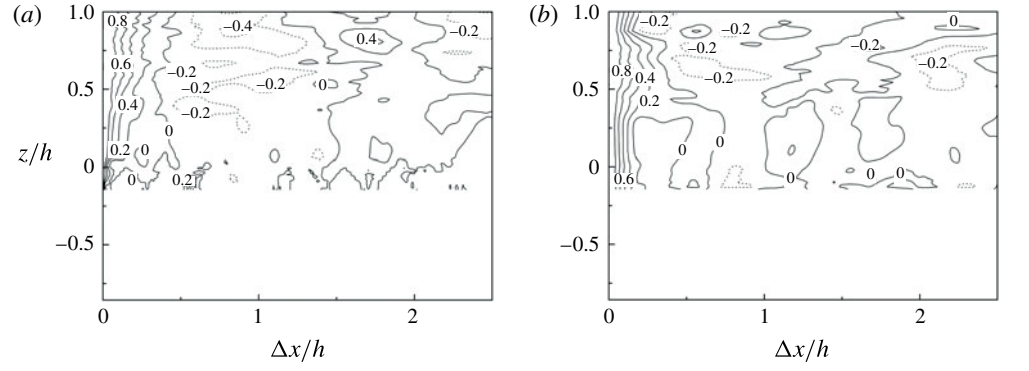

FIGURE 17. Isocontours of the autocorrelation of the pressure as a function of the streamwise spacing $\Delta x/h$, shown across the channel for case H. The solid and dashed lines correspond to positive and negative values, respectively. (*a*) A plane across the top of roughness (i.e. $y/d = 6.5$). (*b*) A plane across the valley of roughness (i.e. $y/d = 6$).

The distance is approximately $0.7h$ (i.e. approximately 690 wall units) for the valley side. This behaviour is associated with the presence of streaks. Since the flow through the valley side is not directly blocked by any roughness, the longer distance is found within the valley plane. It is observed that the correlation distance is much shorter over a rough wall than that over a smooth wall, which is typically a length of the order of 1000 wall units (Breugem *et al.* 2006). This means that the wall roughness makes the size of the coherent structures shorter. Furthermore, the correlation distances of pressure on both sides are much shorter than those of the streamwise velocity, as shown in figure 17.

Like Breugem *et al.* (2006), we use the isocontours of the autocorrelations of streamwise velocity and pressure to investigate the turbulence structures, as shown in figures 18 and 19, respectively. Two typical streamwise planes were adopted to explain the relatively large values of spectra lying in the small- and large-wavenumber regions in figure 15. Figure 18(*a*) corresponds to the top side. It is evident that close

https://doi.org/10.1017/jfm.2018.314 Published online by Cambridge University Press

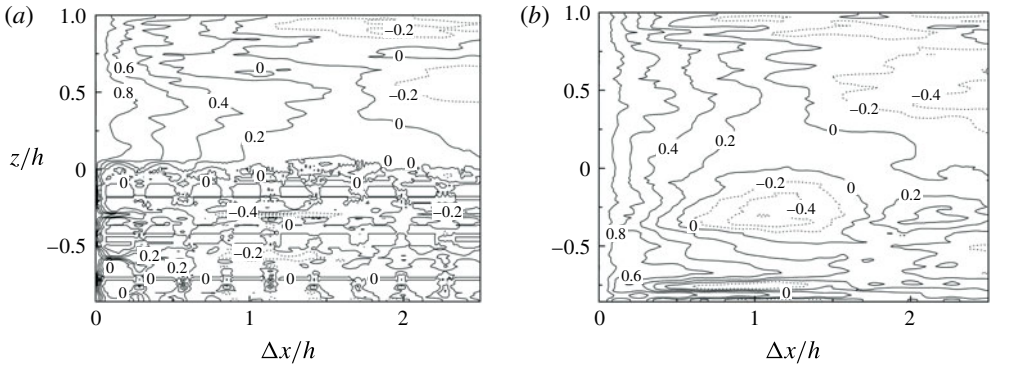

FIGURE 18. Isocontours of the autocorrelation of the streamwise velocity as a function of the streamwise spacing $\Delta x/h$, shown across the channel for case L2. The solid and dashed lines correspond to positive and negative values, respectively. (*a*) A plane across the top of roughness (i.e. $y/d = 6.5$). (*b*) A plane across the valley of roughness (i.e. $y/d = 6$).

to the permeable wall, the correlation distance on the top side of case L2 is much smaller than that on the valley side (i.e. $2h$), as shown in figure 18(*b*), as well as that on the top side over the impermeable bed (i.e. $0.4h$), as shown in figure 16(*a*). The correlation distance close to the wall on the top side is obviously associated with the regularly arranged roughness. It can thus be inferred that turbulent transport across the permeable bed between the roughness increases as compared to the impermeable bed, and the development of elongated structures is prevented. These kinds of small turbulent structures are related to the range with high wavenumbers in the spectra. As for the valley side shown in figure 18(*b*), turbulent structures as large as $2h$ are found close to $z/h = 0$, which are associated with the peak of the streamwise pre-multiplied spectra $E_{uu}k_x$ around $k_x h = 3$. Since all the data in the plane $z/d = 0.01$, i.e. all valley sides, top sides and the positions between them, were used to calculate the pre-multiplied spectra, the spectra for a permeable bed are higher in the region of low and high wavenumbers than those for an impermeable bed. In addition, inside the wall, cell-like patterns are observed on the valley side. This feature is also reflected from the streamwise autocorrelation of the pressure in figure 19(*b*). It corresponds to the presence of the streamwise reciprocal pressure perturbation induced by the KH instability (Kuwata & Suga 2016). It can be observed from the streamwise spectrum of the streamwise velocity that the lengths of the KH structures are approximately $2h$ in the streamwise direction. Besides, inside the bed on the top side, as shown in figure 18(*a*), large-scale structures are found at the same locations on the valley side, but their sizes are limited by the spheres. Additionally, on the valley side, the correlation distance of pressure for case L2 shows a significant increase close to $z/h = 0$ as compared to case H.

The contours of the dimensionless vorticity ω_x^+ ($= \omega_x \upsilon / U_b^2$, where $\omega_x = \partial w'/\partial y - \partial v'/\partial z$) on the yz-plane at $x/d = 12.5$ through the centres of the hemispheres for case H and the large spheres for cases S3 and L2 are presented in figure 20(*a–c*). As the permeability increases, the absolute value of vorticity and the spanwise scale of the turbulence structures in the main flow increases, indicating a larger scale of secondary currents. For permeable beds, significant vorticity is also evident within the bed, illustrating that the turbulence structures can also infiltrate the interface of the spherical particles forming the bed.

https://doi.org/10.1017/jfm.2018.314 Published online by Cambridge University Press

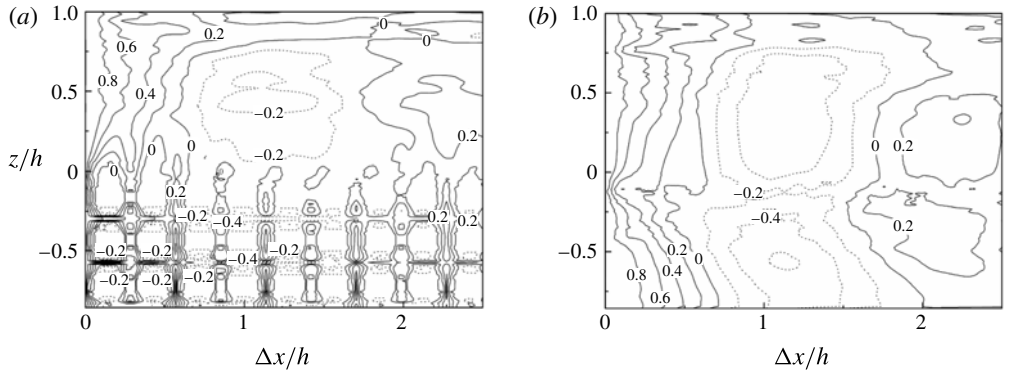

FIGURE 19. Isocontours of the autocorrelation of the pressure as a function of the streamwise spacing $\Delta x/h$, shown across the channel for case L2. The solid and dashed lines correspond to positive and negative values, respectively. (*a*) A plane across the top of roughness (i.e. $y/d = 6.5$). (*b*) A plane across the valley of roughness (i.e. $y/d = 6$).

To verify the extent of fluid infiltration and the streamwise flow structures, the contours of dimensionless instantaneous streamwise velocity u/U_b on the xz-plane at $y/d = 6$ through the valleys formed by the hemispheres for case H and the large spheres for cases S3 and L2 are presented in figure 21(*a–c*). Figure 21(*a*) illustrates that for case H (with an impermeable bed), an inrush of high-speed fluid streaks within the interface of the hemispheres exists near $x/d = 5$ and an outrush of low-speed fluid streaks also appears near $x/d = 9$, but the extent of infiltration is limited. On the other hand, figure 21(*b*,*c*) demonstrates that for cases S3 and L2 (with permeable beds), the flow infiltrates more deeply into the bed, and the extents of infiltration are approximately d and $1.5d$ for cases S3 and L2, respectively. Also, the presence of periodic waves in the streamwise direction indicates that large turbulence structures are getting through the crest level. To quantitatively estimate the flow penetration depth (Brinkman layer thickness) δ_u, the profiles of DA velocity $\langle\bar{u}\rangle$ below the crest were analysed. As shown in figure 22, the DA velocity fluctuates from $z/d \approx -1$ to $z/d \approx -2.6$ for case S3 and from $z/d \approx -0.8$ to $z/d \approx -2.6$ for case L2. All velocity values in those zones are averaged to u_p ($u_p = 0.19u_*$ for case S3 and $u_p = 0.34u_*$ for case L2) with a standard deviation σ ($\sigma = 0.04u_*$ for case S3 and $\sigma = 0.06u_*$ for case L2). The flow penetration depth δ_u is taken as the vertical distance between the crest ($z/d = 0$) and the point at which the difference between the local DA velocity $\langle\bar{u}\rangle$ and u_p decays to 1 % of the DA velocity at the crest (u_c), i.e. $\langle\bar{u}\rangle_{z=-\delta_u} = 0.01(u_c - u_p) + u_p$. Then, the flow penetration depths δ_u are calculated as $-1.09d$ for case S3 and $-1.3d$ for case L2.

The DA Reynolds shear stresses are used to quantify the penetration depth δ_{rss}, which is defined as $-\langle\overline{u'w'}\rangle_{z=-\delta_{rss}} = 0.01(-\langle\overline{u'w'}\rangle)_{max}$, where $(-\langle\overline{u'w'}\rangle)_{max}$ is the maximum DA Reynolds shear stress around the crest. Then, the penetration depths of turbulent shear stress δ_{rss} are calculated as $-1.06d$ for case S3 and $-1.52d$ for case L2, as shown in figure 23.

Figure 24(*a–c*) presents the contours of dimensionless instantaneous streamwise velocity u/U_b and dimensionless Reynolds shear stress $\overline{u'w'}/u_*^2$ on a yz-plane at $x/d = 12$ for cases H, S3 and L2. Vanderwel & Ganapathisubramani (2015) illustrated that the streamwise continuity of the surface topology was an important factor in the locations of low- and high-momentum pathways. The gap between two neighbouring

https://doi.org/10.1017/jfm.2018.314 Published online by Cambridge University Press

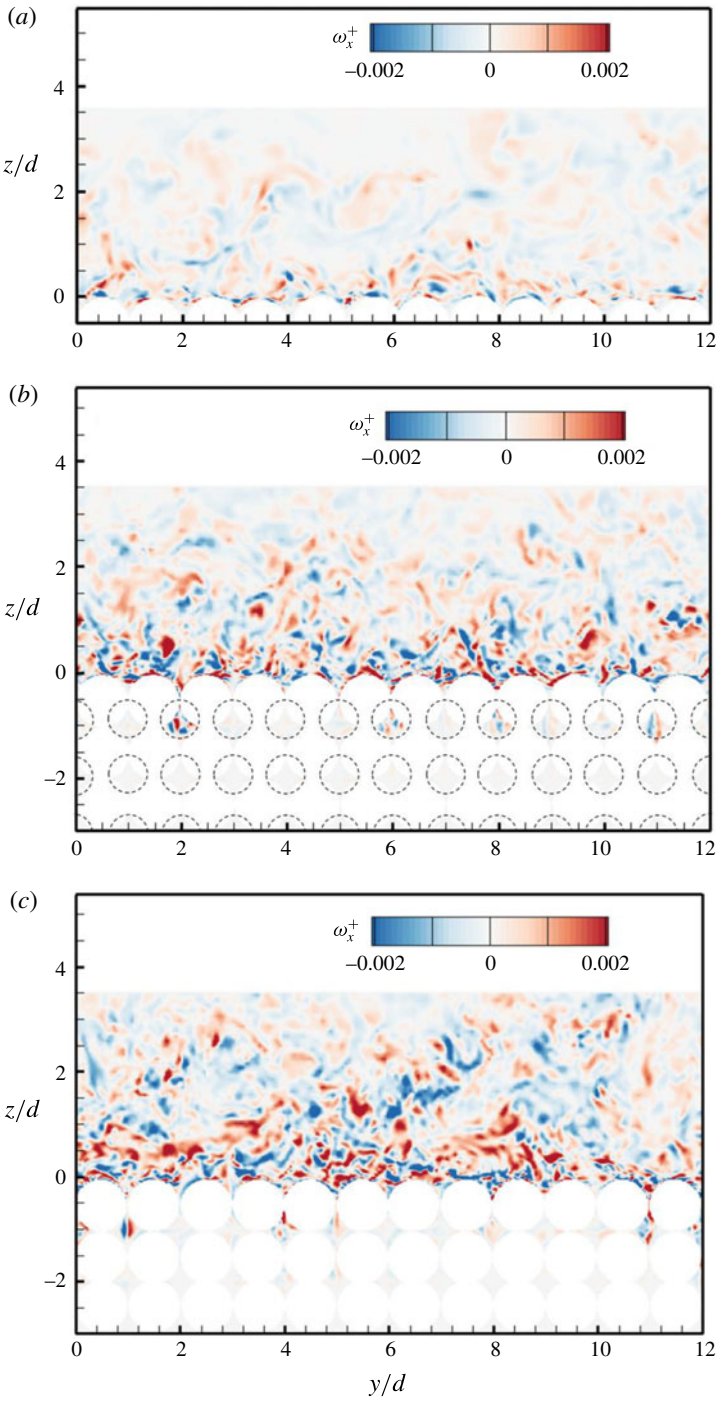

FIGURE 20. (Colour online) Contours of dimensionless vorticity ω_x^+ on the yz-plane at $x/d = 12.5$ through the centres of hemispheres for (*a*) case H and large spheres for (*b*) case S3 and (*c*) case L2. The dotted line in case S3 shows the periphery of small spheres ($d' = 0.73d$).

https://doi.org/10.1017/jfm.2018.314 Published online by Cambridge University Press

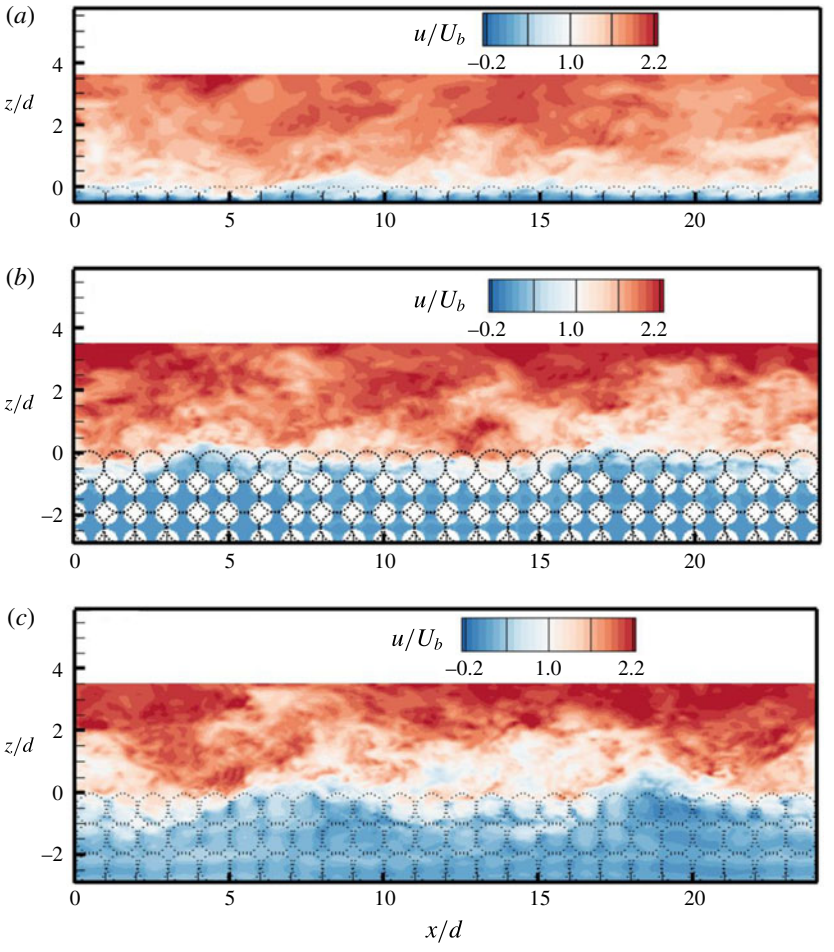

FIGURE 21. (Colour online) Contours of dimensionless instantaneous streamwise velocity u/U_b on the xz-plane at $y/d = 6$ through the valleys formed by hemispheres for (a) case H and large spheres for (b) case S3 and (c) case L2. The dotted line shows the periphery of hemispheres or large spheres.

hemispheres or spheres in the streamwise direction was considered to be d for the three cases. It was less than the length of the separation zone behind a barrier which is known to be approximately 2–2.5d. So, the closely packed hemispheres or spheres acted like a continuous strip and exhibit a low momentum pathway, which is comparable to previous experiments focusing on the flow over elevated roughness strips. Anderson *et al.* (2015) conducted experiments in a wind tunnel and showed that the spanwise-vertical anisotropy of the Reynolds shear stress contributed to the production of time-averaged streamwise vorticity. In case H (with an impermeable bed), the low-velocity zones, which correspond to low-momentum pathways, are in the vicinity of the crests of the hemispheres, whereas in general, the flow between the hemispheres forms relatively high-momentum pathways. In the inset of figure 24(a), it is apparent that the Reynolds shear stress is enhanced over the crests of the hemispheres (low-momentum pathways) and is weakened within the valleys (high-momentum pathways). With the limited width of the spanwise-alternate

https://doi.org/10.1017/jfm.2018.314 Published online by Cambridge University Press

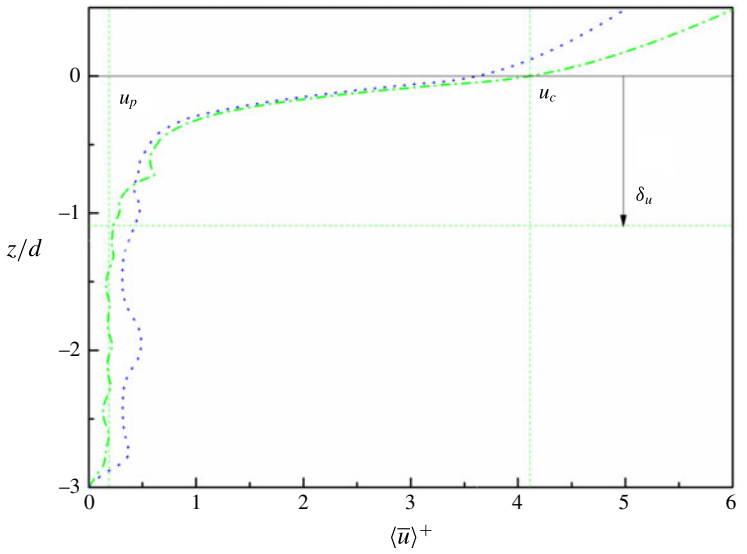

FIGURE 22. (Colour online) DA streamwise velocity below the crest for case S3 (green dashed-dotted line) and case L2 (blue dotted line). δ_u is the flow penetration depth (Brinkman layer thickness), u_p is the vertically averaged velocity below the Brinkman layer, u_c is the DA velocity at the crest. Values of δ_u, u_p and u_c are only shown for case S3.

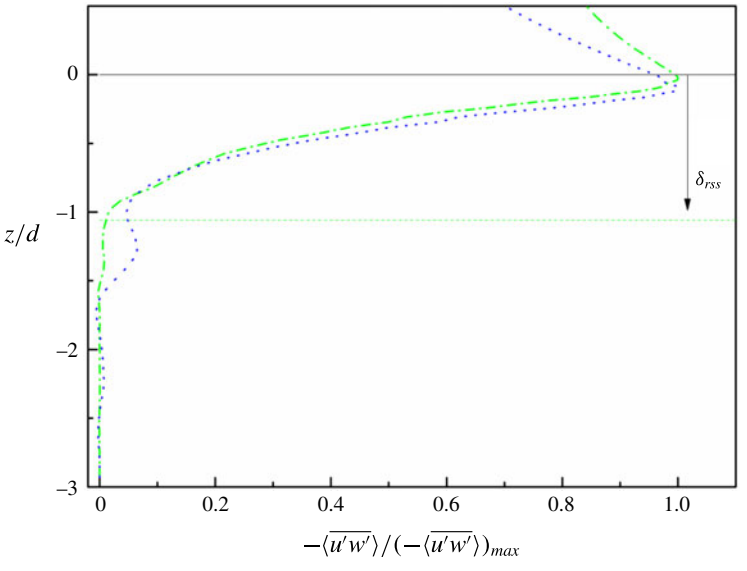

FIGURE 23. (Colour online) DA Reynolds shear stress normalized by the maximum shear stress around the crest for case S3 (green dashed-dotted line) and case L2 (blue dotted line). δ_{rss} is the shear stress penetration depth for case S3.

strips of shear stress, time-averaged secondary currents can only develop near the crest, as shown in figure 12(*a*). As discussed before, with an increase in permeability, the vertical velocities within the valley formed by the spheres become stronger.

https://doi.org/10.1017/jfm.2018.314 Published online by Cambridge University Press

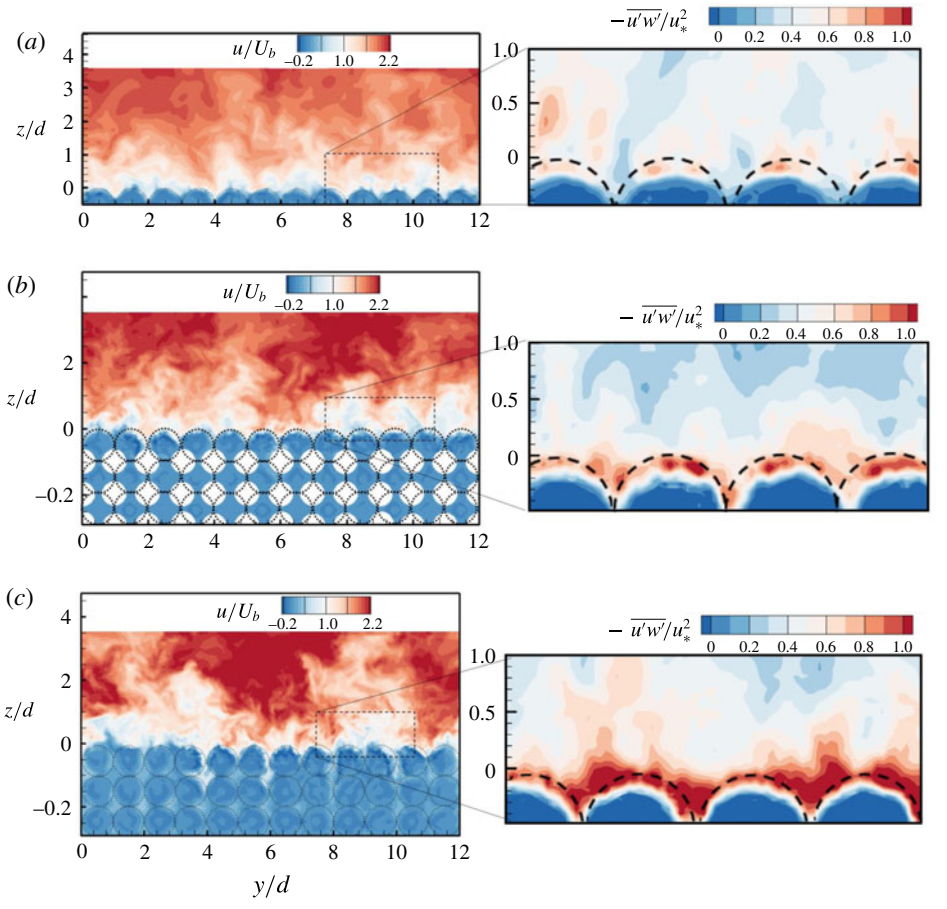

FIGURE 24. (Colour online) Contours of dimensionless instantaneous streamwise velocity u/U_b and dimensionless Reynolds shear stress $\overline{u'w'}/u_*^2$ on a yz-plane at $x/d = 12$ through the valleys formed by hemispheres for (*a*) case H and large spheres for (*b*) case S3 and (*c*) case L2. The dotted line shows the periphery of hemispheres or large spheres. The enlarged views of the flow zones near the crest are shown in insets.

This leads to a high shear stress zone as well as a low-momentum pathway within the valley, which connects the adjacent high shear stress zones over the crests of the spheres, as shown in figure 24(*b*,*c*). Therefore, as the permeability is higher, a wider extended (connected) high spanwise-alternate shear stress strip is obtained for case S3 and case L2. The extended high shear stress strips act as wider spanwise-alternate roughness strips, causing large time-averaged secondary currents in figure 12(*b*,*c*).

4.5. *Quadrant analysis of velocity fluctuations*

The quadrant analysis of Lu & Willmarth (1973) was employed to identify the presence of coherent structures located at different elevations and to quantify their contributions to the Reynolds shear stress. To perform the quadrant analysis, the velocity fluctuations, u' and w', are plotted and divided into four quadrants based on the signs of their instantaneous values. Figure 25(*a–l*) shows the contours of the turbulent probability density function (PDF) of dimensionless velocity fluctuations,

https://doi.org/10.1017/jfm.2018.314 Published online by Cambridge University Press

u'/u_* and w'/u_*, at different elevations z/d located on the line of intersection of two vertical planes $x/d = 12$ and $y/d = 6$. We choose the location of the points in such a way so that the line of intersection is not blocked by the hemispheres or spheres. In the quadrant analysis, the first quadrant $Q1$ corresponds to u', $w' > 0$, called the outward intersection events; the second quadrant $Q2$ to $u' < 0$, $w' > 0$, called the ejection events; the third quadrant $Q3$ to u', $w' < 0$, called the inward intersection events; and the fourth quadrant $Q4$ to $u' > 0$, $w' < 0$, called the sweep events. Therefore, the ejection events $Q2$ transport a low-momentum fluid upwards away from the bed, while the sweeping events $Q4$ transport a high-momentum fluid downwards towards the bed. The ejection–sweep phenomenon results in intermittent flushing of dead flow that accumulates within the roughness elements (Grass, Stuart & Mansour-Tehrani 1991). Figure 25(*a*,*d*) shows that the vertical fluctuations w' are relatively small below the crest in case H, and the fluid motion is mainly due to streamwise velocity fluctuations u'. As the bed becomes more permeable (from cases 1 to 3), the vertical velocity fluctuations w' increase below the crest, which is apparent from figure 25(*a–e*). This is consistent with figure 6, where the recirculation zone between the hemispheres shows a weak vertical fluid intrusion into the bed, while the fluid intrusion is obviously enhanced over the permeable beds. As the intensity of vertical fluctuations w' influences the vertical momentum transport, we can infer that within the valley, the Reynolds shear stress increases with an increase in bed permeability, corresponding to the change of momentum pathways, as shown in figure 24. Moreover, the relatively small vertical fluctuations w' result in a weak ejection–sweep phenomenon below the bed. It represents the lack of intermittent flushing and causes a dead-flow zone between the hemispheres in case H. At the crest bed level, the slopes of the PDF in case S3 and case L2 are larger than that in case H, as shown in figure 25(*g–i*), illustrating larger vertical fluctuations w' over permeable beds. With an increase in elevation, statistically significant variations are noticeable between ejection and sweep events for permeable beds. The ejection and sweep events in deep locations are small and almost equal, as shown in figure 25(*b*,*c*), indicating an isotropic zone within the interfacial layer. Slightly below the crest, the ejection events are dominant, as shown in figure 25(*e*,*f*), transporting low-momentum fluid away from the bed. As the elevation becomes higher, the sweep events seem to be enhanced in figure 25(*h*,*i*). Suga *et al.* (2010, 2011) and Suga (2016) also revealed that the contribution from sweep events near porous media becomes more dominant, while that from ejection events tends to lose its strength. Further away from bed, the ejection and sweep events are almost identical again, as shown in figure 25(*k*,*l*).

4.6. *Turbulent kinetic energy budget*

The expression for the TKE budget was derived by Raupach, Antonio & Rajagopalan (1991) for flow over canopies and Mignot *et al.* (2009*b*) for flow over macro-roughness (gravel bed). The DA TKE budget for flow over a gravel bed is given by

$$\underbrace{-\langle\overline{u_i'w'}\rangle\frac{\partial\langle\bar{u}_i\rangle}{\partial z}}_{P} \underbrace{-\langle\overline{u_i'u_j'}\rangle\left\langle\frac{\partial\tilde{u}_i}{\partial x_j}\right\rangle}_{P_m} \underbrace{-\left\langle u_i'u_j'\cdot\frac{\partial\tilde{u}_i}{\partial x_j}\right\rangle}_{P_w}$$
$$= \underset{\text{dissipation}}{\underset{\text{TKE}}{\langle\varepsilon\rangle}} + \underbrace{\frac{\partial\langle\overline{k'w'}\rangle}{\partial z}}_{F_k} + \underbrace{\frac{\partial\langle\tilde{k}\tilde{w}\rangle}{\partial z}}_{F_w} + \underbrace{\frac{1}{\rho}\frac{\partial\langle\overline{p'w'}\rangle}{\partial z}}_{P_d} - \underbrace{\upsilon\frac{\partial^2\langle k\rangle}{\partial z^2}}_{\upsilon_d}, \tag{4.3}$$

https://doi.org/10.1017/jfm.2018.314 Published online by Cambridge University Press

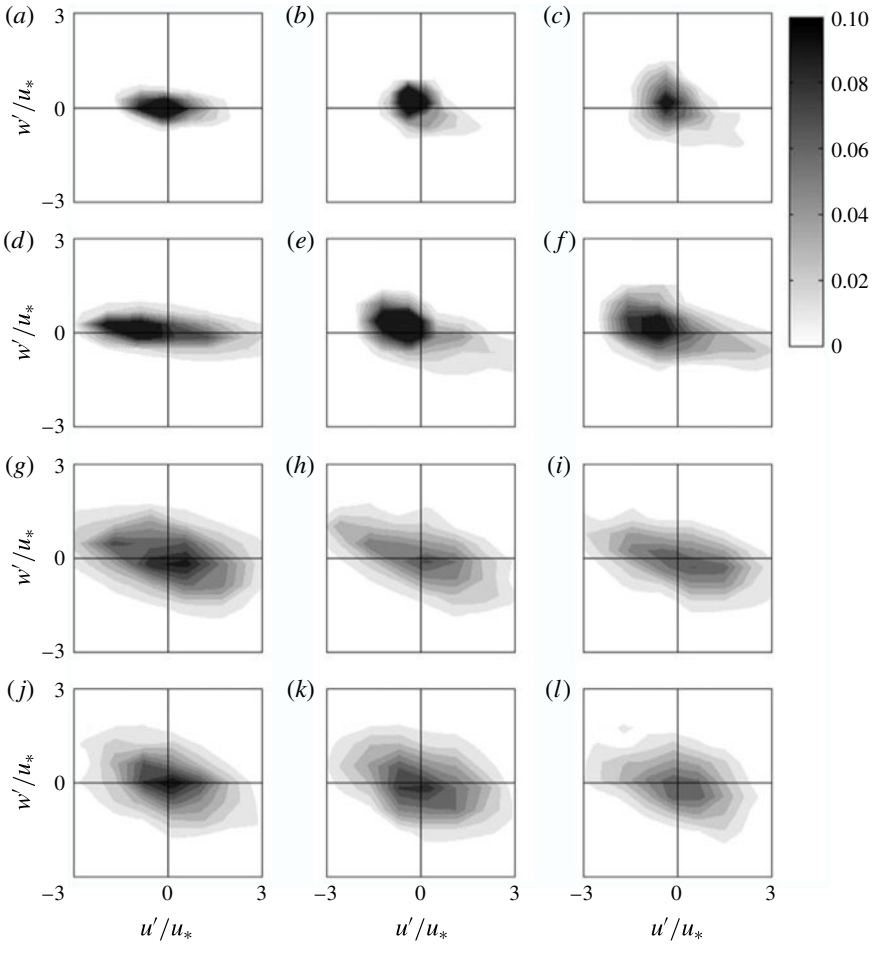

FIGURE 25. Quadrant analysis of probability density functions (PDFs) of dimensionless velocity fluctuations, u'/u_* and w'/u_*, at different elevations z/d located on the line of intersection of two vertical planes $x/d = 12$ and $y/d = 6$. (*a–c*) $z/d = -0.4$, (*d–f*) $z/d = -0.2$, (*g–i*) $z/d = 0$ and (*j–l*) $z/d = 0.5$. (*a*,*d*,*g*,*j*) are case H, (*b*,*e*,*h*,*k*) are case S3 and (*c*,*f*,*i*,*l*) are case L2.

where P is the TKE production rate resulting from the DA velocity against the DA shear, P_m and P_w are the TKE production rates due to velocity fluctuations against the DA shear stress and FISS, respectively, ε is the TKE dissipation rate, F_k and F_w are the TKE diffusion and form-induced diffusion rates, respectively, $k' = u_i' u_i'/2$, $k = \overline{k'}$, and P_d and v_d are the pressure energy diffusion and the viscous dissipation rates, respectively. The viscous dissipation rate can be discarded due to its minimal contribution to the TKE budget as compared to other terms over the entire flow depth. Mignot *et al.* (2009*b*) found that P_m and P_w were lower than 5 % of the TKE production rate P, while Raupach *et al.* (1991) found that P_w was significant below the crest. Lopez & Garcia (1999) obtained the numerical results from a k–ε model and found that P_w could be twice as large as P within the roughness layer. In this study, altogether 18 TKE production rate terms P_m and P_w (nine for each bed-type-induced terms P_m and P_w) were calculated. We found that the sum of them

https://doi.org/10.1017/jfm.2018.314 Published online by Cambridge University Press

was higher than 10 % of P and they could not be neglected. Moreover, the terms $\langle\overline{u'u'}\rangle\langle\partial\tilde{u}/\partial x\rangle$ and $\langle\overline{u'w'}\rangle\langle\partial\tilde{u}/\partial z\rangle$ account for more than 85 % of the total P_m for three cases, while there is no significant dominance for P_w values.

According to the Kolmogorov similarity hypothesis (Kolmogorov 1941), the turbulence statistics in a small-scale universal equilibrium range can be uniquely determined by the kinematic viscosity of the fluid and turbulent dissipation rate as

$$\langle\varepsilon\rangle = 2\upsilon\langle\overline{s_{ij}s_{ij}}\rangle \tag{4.4}$$

$$s_{ij} = \frac{1}{2}\left(\frac{\partial u_i'}{\partial x_j} + \frac{\partial u_j'}{\partial x_i}\right). \tag{4.5}$$

Using the three-dimensional velocity fluctuations, the TKE dissipation rate in LES can be calculated more accurately than the experimental data sampling at a point, as done by Mignot *et al.* (2009*a*).

In dimensionless form, the terms of the TKE budget are expressed as T_P, E_D, T_D, $P_D = (P + P_m + P_w, \varepsilon, F_{k+}F_w, P_d) \times (h/u_*^2)$. The DA pressure energy diffusion rate is calculated as $\langle P_D\rangle = \langle T_P\rangle - \langle E_D\rangle - \langle T_D\rangle$. A comprehensive picture of the variations of the terms of the DA TKE budget in the vicinity of the crest for the three cases is shown in figure 26(*a–c*). In the three cases, the $\langle T_P\rangle$ reaches a maximum value slightly below the crest, $z/d = -0.1$, which is in conformity with Mignot *et al.* (2009*a*) and Lopez & Garcia (1999). Below this level, $\langle T_P\rangle$ decreases towards a value close to zero for $z/d = -0.5$, as shown in figure 26(*a*), and for $z/d = -1$, as shown in figure 26(*b*,*c*). Considering the turbulent diffusion terms, the $\langle T_D\rangle$-profiles possess two peaks for the three cases. By examining the F_k- and F_w-values, it is observed that the upper peak is mostly attributed to the turbulent diffusion rate F_k and the other is to the form-induced diffusion rate F_w. Furthermore, F_k accounts for more than 80 % of the upper peak for three cases. With an increase in permeability, the contributions from F_k are 8 %, 39 % and 50 % of the lower peak of $\langle T_D\rangle$, indicating that the turbulence can reach deeper within the bed.

There are three typical layers defined by the terms of the TKE budget: namely, the equilibrium layer, the form-induced sublayer and the interfacial sublayer. In the equilibrium layer, the TKE production rate nearly balances the turbulent dissipation rate and the diffusion rate is generally found to be negligible (Mignot *et al.* 2009*a*). The layer of high TKE production rates, exceeding the dissipation rates significantly, is called the form-induced sublayer, since the macro-roughness creates a strong, detached mixing-type flow over the crest. The TKE diffusion rates are positive in the form-induced sublayer, transporting TKE upwards and downwards. Towards the bed, in the lower part of the roughness sublayer, called the interfacial sublayer, the flow is characterized by a balance between a low dissipation rate and a low TKE production rate. In figure 26(*d*), the TKE diffusion rates are compared among the cases, as they can be used to determine the thickness of the form-induced sublayer. The form-induced sublayer is very thin, with an extent from $-0.20d$ to $0.04d$ for case H. For case S3 (with a permeable bed), this layer becomes thicker and the layer extends from $-0.36d$ to $0.25d$. For case L2 (with a permeable bed, having a permeability greater than that for case S3), the extent of the form-induced sublayer extends from $-0.36d$ to $0.82d$, indicating a significant influence of permeability on the flow near the bed. Within the interfacial sublayer, the pressure diffusion rate $\langle P_D\rangle$ compensates for the turbulent diffusion rate, which is consistent with previous experimental results (Mignot *et al.* 2009*a*).

https://doi.org/10.1017/jfm.2018.314 Published online by Cambridge University Press

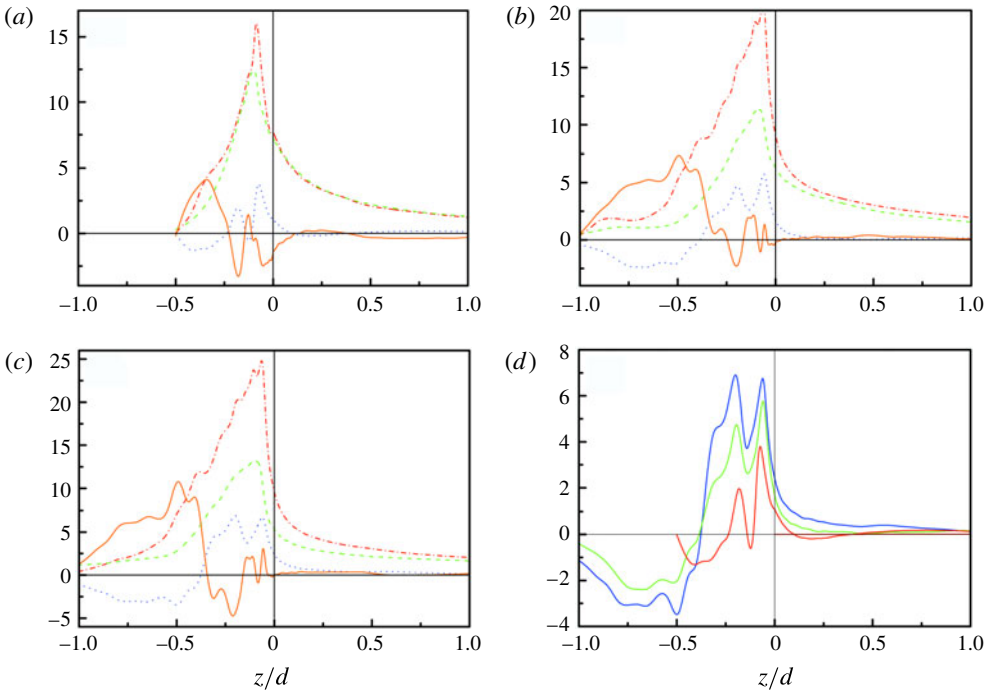

FIGURE 26. (Colour online) The DA TKE budget for (*a*) case H, (*b*) case S3 and (*c*) case L2. $\langle T_P \rangle$ (red dashed-dotted line), $\langle E_D \rangle$ (green dashed line), $\langle T_D \rangle$ (blue dotted line) and $\langle P_D \rangle$ (orange solid line). (*d*) $\langle T_D \rangle$ for case H (red line), case S3 (green line) and case L2 (blue line).

4.7. *Flow quantities around the crest*

As the flow around the crest plays an important role in the transport process and the flow within the bed is difficult to measure experimentally, we choose several typical flow quantities – namely, the flow penetration depth (Brinkman layer thickness), the shear stress penetration depth and the form-induced sublayer thickness – to show their relationships with Re_K. The inner scales (υ/u_*) and mean diameter of sediments (d_p) are used to normalize these flow quantities. All simulated results over permeable beds (case S1–S5 and case L1–L3) are presented here.

Figure 27 shows the DA velocity and shear stress profiles for eight cases around the crest. Ghisalberti & Nepf (2002) pointed out that in a turbulent flow over a fairly dense canopy, the inflection of the mean velocity profile was susceptible to the KH instabilities. From figure 27(*a*), it is apparent that the mean velocity profiles exhibit such an inflection below the crest within permeable beds. According to Rayleigh's criterion (Drazin & Reid 1981), it is an essential condition for an inviscid instability. In addition, the mean velocity profiles exhibit a decreasing trend at the crest and an increasing trend within the bed with an increase in Re_K. Using the same method as shown in figures 22 and 23, the flow penetration depths δ_u and the shear stress penetration depths δ_{rss} for eight permeable cases are calculated and shown in figure 28, which are normalized by υ/u_* and d_p. The thickness of flow penetration depth (Brinkman layer thickness) can be traditionally described as dependent on the bed permeability (Boudreau 2001; Goyeau *et al.* 2003). However, Goharzadeh, Khalili

https://doi.org/10.1017/jfm.2018.314 Published online by Cambridge University Press

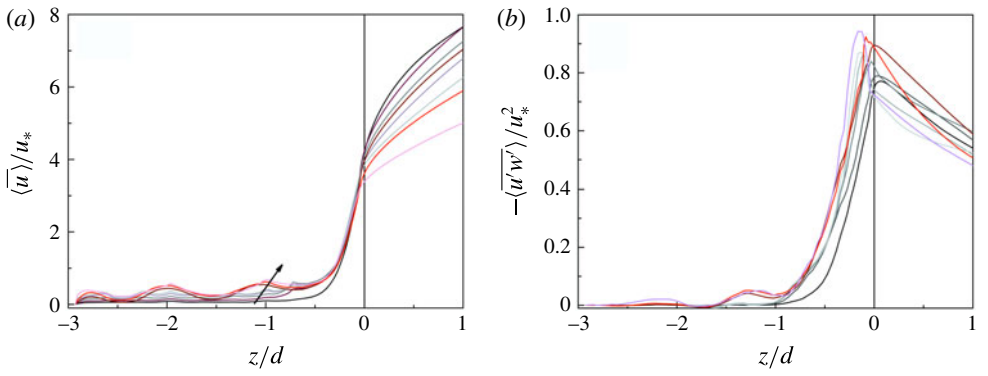

FIGURE 27. (Colour online) (*a*) The DA velocity profiles and (*b*) DA Reynolds shear stress profiles for eight cases of permeable beds (S1–S5, from black to grey, respectively, and L1–L3, from wine to pink, respectively; lines become lighter with an increase in Re_K).

& Jørgensen (2005) concluded that the Brinkman layer thickness is of the same order of magnitude as the sediment diameter. In this study, we find a similar conclusion as that of Goharzadeh *et al.* (2005). Figure 28(*a*) demonstrates that the values of the Brinkman layer thickness lie between $0.8d_p$ and $1.3d_p$ for Re_K $O(1–10)$. Moreover, as Re_K increases beyond unity, the flow penetration depth normalized by the mean particle diameter becomes deeper. In contrast, for highly permeable beds, the flow penetration depth appears to stay around $1.3d_p$ with Re_K. This kind of feature may be caused by the methodology used to estimate the critical point $\langle \bar{u} \rangle_{z=-\delta_u}$ and it can be explained by the magnitude of u_p in bed. For a bed with low bed permeability, u_p is quite low as a result of the low bed permeability and flow energy (u_*). The change of u_* mainly affects u_c and leads to a decreasing trend of u_c and an increasing trend of u_p with an increase in u_* (u_c and u_p are both normalized by u_*). As the change of u_c is more obvious than u_p for a bed with low permeability and u_* (which jointly lead to low Re_K), according to $\langle \bar{u} \rangle_{z=-\delta_u} = 0.01(u_c - u_p) + u_p$, the increase in u_* over a bed with low permeability leads to a limited increase or slight decrease of the critical velocity $\langle \bar{u} \rangle_{z=-\delta_u}$, which results in deeper flow penetration. For a bed with higher Re_K, u_p increases more significantly than that over a bed with low Re_K. The combined effects of an increase in u_p and a decrease in u_c cause an obvious increase in $\langle \bar{u} \rangle_{z=-\delta_u}$, which pushes the critical point closer to the crest. So the flow penetration depth shows a minor difference for high Re_K. For the shear stress penetration depth δ_{rss}, it increases to $1.2d_p$ over a permeable bed with small d_p, i.e. case S1–S5, which is comparable to the Brinkman layer thickness δ_u. On the other hand, for a permeable bed with large d_p, i.e. L1–L3, the shear stress penetration depth reaches $1.6d_p$, which is caused by the larger pore space between the sphere layers around $z/d = -1$ in cases L1–L3. When the inner scale is adopted in figure 28(*b*), it shows that except separation behaviour between the cases of different bed configurations, both the flow penetration depth and shear stress penetration depth increase with Re_K. For $Re_K < 20$, the two kinds of penetration depths are similar, while for $Re_K > 20$, the shear stress penetration depth becomes larger than flow penetration depth, with a maximum ratio of 1.4 times at $Re_K = 109$. As discussed before, u_* has some effect on the determination of the critical velocity $\langle \bar{u} \rangle_{z=-\delta_u}$; so we infer that when the penetration depth is normalized by the inner scale, the flow energy (i.e. u_*) is considered, which leads to a dependence of δ^+ on Re_K.

https://doi.org/10.1017/jfm.2018.314 Published online by Cambridge University Press

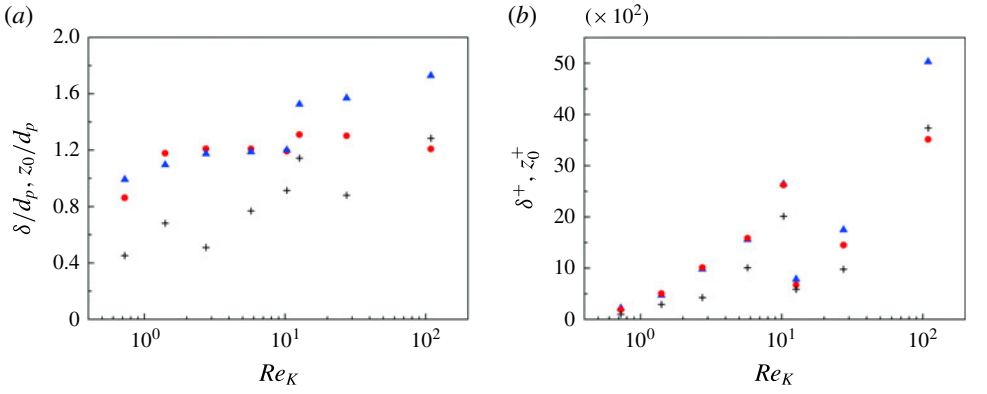

FIGURE 28. (Colour online) The Re_K dependence of flow penetration depth δ_u (red dot), shear penetration depth δ_{rss} (blue triangle) and displacement height z_0 (black cross) normalized by (*a*) d_p and (*b*) υ/u_*. δ represents the penetration depth, i.e. δ_u and δ_{rss}. $\delta^+ = \delta u_*/\upsilon$ and $z_0^+ = z_0 u_*/\upsilon$.

Based on the drag force acting within the porous medium (Jackson 1981), Clifton *et al.* (2008) argued that the displacement height is a length scale related to the shear penetration depth. We compare the normalized displacement height z_0/d_p with the penetration depth δ/d_p in figure 28(*a*), and z_0^+ with δ^+ in figure 28(*b*). It shows that the trend of z_0/d_p with Re_K is not consistent with that of δ/d_p with Re_K. However, when the inner scale was adopted, their trends become more similar. In addition, the ratio of displacement height to penetration depth is approximately 0.46–0.75, which approximates to the theoretical value of 0.5.

Based on the criterion that the thickness of the form-induced sublayer δ_f can be determined from the elevation at which the TKE diffusion rate $\langle T_D \rangle$ attains a small finite value ($\langle T_D \rangle > 0$), δ_f is calculated for all permeable beds. As shown in figure 29(*a*), δ_f normalized by the mean diameter increases around $Re_K = 1$ and tends to become constant at 1.2 when Re_K is $O(10)$. In figure 29(*b*), the relationship between δ_f^+ (which is normalized by υ/u_*) and Re_K shows similar trends to the penetration depth. In addition, the ratio of the displacement height to the form-induced layer thickness is approximately 0.66–1.28.

5. Conclusions

To investigate the effects of permeability on hydraulically macro-rough flow, LES was carried out for open-channel flow over three kinds of macro-rough beds. They were closely packed hemispheres, three closely packed layers of spheres with small spheres inset within the interspace of the spheres, and the similar three layers of spheres without any small spheres. In order to distinguish the effects of the permeability of macro-rough beds, the values of the surface roughness of the three cases were set identical. A combination of canonical flow typologies is represented in terms of permeability Reynolds number, Re_K, which ranges from an impermeable bed ($Re_K = 0$) to a highly permeable bed ($Re_K = 109$). A DA technique was applied to study the spatial disturbance of time-averaged flow and the turbulence characteristics.

For the simulated results, the log law was fitted to the DA velocity over the crest level of bed roughness. The values of the von Kármán constant, the equivalent roughness height and the zero-displacement height were obtained from the fitted log

https://doi.org/10.1017/jfm.2018.314 Published online by Cambridge University Press

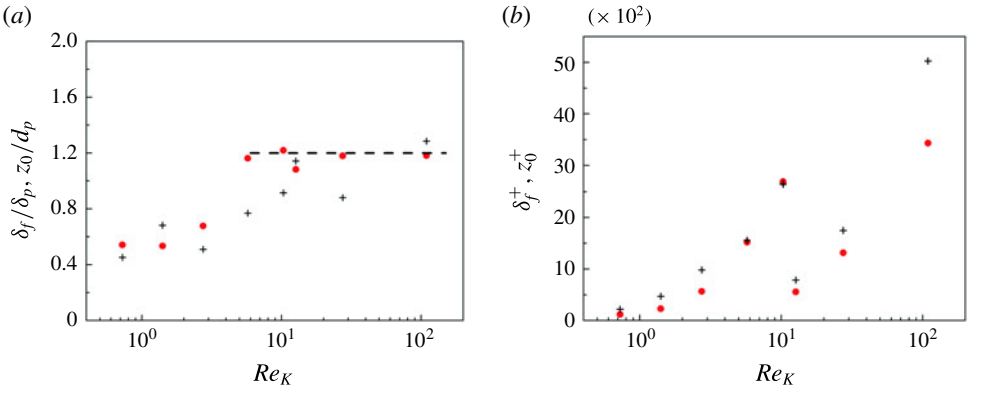

FIGURE 29. (Colour online) The Re_K dependence of the form-induced sublayer thickness δ_f (red dot) and displacement height z_0 (black cross) normalized by (*a*) d_p and (*b*) υ/u_*. $\delta_f^+ = \delta_f u_*/\upsilon$ and $z_0^+ = z_0 u_*/\upsilon$.

law for the different cases. For the impermeable bed, their values agree well with their traditional values for fully rough flow, whereas with an increase in bed permeability, smaller values of the von Kármán constant, larger values of the equivalent roughness height and the zero-displacement height are obtained, as compared to their traditional values for fully rough flow.

It is revealed that the structure and dynamics of turbulence are significantly influenced by the bed permeability. The vortex shedding becomes deeper within the permeable bed, causing more intense vertical velocity fluctuations as well as bursting events within the bed. As a result of the effects of wall-blocking, fluid infiltration is prevented within the impermeable bed, leading to a strong recirculation zone within the valley formed by the hemispheres. This dead-flow zone is due to a lack of the intermittent flushing causing low Reynolds normal stresses. However, the streamwise form-induced normal stress increases in this zone, because the recirculation is more stable with time and has a strong influence on the heterogeneity of the streamwise time-averaged flow. The contribution from the form-induced turbulent diffusion rate also increases within the bed. In the streamwise direction, coherent structures which are 0.4–1.3h long are more prevalent over an impermeable bed, while structures which are larger than 1.3h or smaller than 0.4h are more predominant over a permeable bed. With the discussion on isocontours of the autocorrelations of streamwise velocity and pressure, it can be inferred that on the top side, the shortening of turbulent structures close to a permeable bed is associated with the weakening effects of wall-blocking and turbulent transport across the bed interface. Also, on the valley side, large-scale structures as long as 2h can develop close to the bed due to the KH-type instability and the absence of sphere blocking.

The effects of the spanwise time-averaged secondary currents on the DA momentum flux balance and the mechanism of turbulent secondary currents are also investigated in this study. For the permeable bed, the spanwise secondary currents transport high momentum to the inner flow region and bring low momentum to the outer flow region. It causes the profiles of the DA Reynolds shear stress to detach the gravity line at certain elevation away from the bed, where the heterogeneity of time-averaged flow in the spanwise direction causes the DA form-induced shear stresses attain their peaks. This is an interesting feature in that the DA form-induced shear stress

https://doi.org/10.1017/jfm.2018.314 Published online by Cambridge University Press

is not negligible away in the main flow region and the secondary currents are the main reason. The vertical Reynolds normal stress near a more permeable bed is dominated by relatively large vortical structures, which are responsible for the exchange of momentum between the top layer of the bed and the main flow. The exchange of momentum induces a strong increase in the Reynolds shear stress within the valley formed by the roughness elements, connecting the adjacent peaks of the Reynolds shear stress near the crests of roughness elements. The spanwise scale of the combined high Reynolds shear stress zone increases with increasing permeability and acts as a wider roughness strip, resulting in the formation of larger turbulent secondary currents in the main flow.

The Re_K dependence of several flow quantities around the crest is analysed. The Brinkman layer thickness is of the same order of magnitude as the mean particle diameter. Comparing with the normalization by mean diameter, the flow and shear stress penetration into the bed normalized by the inner scale (υ/u_*) suggest a better correlation with Re_K, which is attributed to the inclusion of the flow energy. The form-induced sublayer thickness normalized by mean diameter increases with $Re_K \sim O(1)$. However, it becomes nearly constant and independent of Re_K as it approaches $Re_K \sim O(10)$. When it is normalized by υ/u_*, the trend becomes similar to that of the penetration depth. The displacement height is quantitatively compared with the penetration depth and form-induced thickness. The ratio of displacement height to penetration depth is approximately 0.46–0.75, and the ratio of displacement height to form-induced layer thickness is approximately 0.66–1.28.

Acknowledgements

This investigation was supported by the National Natural Science Foundation of China (no. 91647210, 11372161), National Key Research and Development Program of China (no. 2016YFC0402506) and 111 Project (no. B18031).

REFERENCES

AMIR, M., NIKORA, V. I. & STEWART, M. T. 2014 Pressure forces on sediment particles in turbulent open-channel flow: a laboratory study. *J. Fluid Mech.* **757**, 458–497.

ANDERSON, W., BARROS, J. M., CHRISTENSEN, K. T. & AWASTHI, A. 2015 Numerical and experimental study of mechanisms responsible for turbulent secondary flows in boundary layer flows over spanwise heterogeneous roughness. *J. Fluid Mech.* **768**, 316–347.

BEAVERS, G. S. & JOSEPH, D. D. 1967 Boundary conditions at a naturally permeable wall. *J. Fluid Mech.* **30**, 197–207.

BOMMINAYUNI, S. & STOESSER, T. 2011 Turbulence statistics in an open-channel flow over a rough bed. *J. Hydraul. Engng* **137** (11), 1347–1358.

BOUDREAU, B. P. 2001 Solute transport above the sediment–water interface. In *The Benthic Boundary Layer: Transport Processes and Biogeochemistry* (ed. B. P. Boudreau & B. B. Jorgensen), pp. 104–126. Oxford University Press.

BREUER, M. A. & RODI, W. 1994 Large-eddy simulation of turbulent flow through a straight square duct and a 180° bend. In *Direct and Large-Eddy Simulation I* (ed. P. R. Voke, L. Kleiser & J. P. Chollet), pp. 273–285. Kluwer.

BREUGEM, W. P., BOERSMA, B. J. & UITTENBOGAARD, R. E. 2006 The influence of wall permeability on turbulent channel flow. *J. Fluid Mech.* **562**, 35–72.

CALMET, I. & MAGNAUDET, J. 1997 Large-eddy simulation of high-Schmidt number mass transfer in a turbulent channel flow. *Phys. Fluids* **9** (2), 438–455.

CASTRO, I. P., CHENG, H. & REYNOLDS, R. 2006 Turbulence over urban-type roughness: decutions from with tunnel measurements. *Boundary-Layer Meteorol.* **118** (1), 109–131.

https://doi.org/10.1017/jfm.2018.314 Published online by Cambridge University Press

CHAITANYA, D. G. & SOURABH, V. A. 2016 DNS study of particle-bed-turbulence interactions in an oscillatory wall-bounded flow. *J. Fluid Mech.* **792**, 232–251.

CLIFTON, A., MANES, C., RÜEDI, J. D., GUALA, M. & LEHNING, M. 2008 On shear-driven ventilation of snow. *Boundary-Layer Meteorol.* **126** (2), 249–261.

COCEAL, O., DOBRE, A., THOMAS, T. G. & BELCHER, S. E. 2007 Structure of turbulent flow over regular arrays of cubical roughness. *J. Fluid Mech.* **589**, 375–409.

COLEMAN, S. E., NIKORA, V. I., MCLEAN, S. R. & SCHLICKE, E. 2007 Spatially averaged turbulent flow over square ribs. *J. Engng Mech.* **133** (2), 194–204.

DEFINA, A. 1996 Transverse spacing of low-speed streaks in a channel flow over a rough bed. In *Coherent Flow Structures in Open Channels* (ed. P. J. Ashworth, S. J. Bennett, J. L. Best & S. J. McLelland), pp. 87–99. Wiley.

DEY, S. & DAS, R. 2012 Gravel-bed hydrodynamics: double-averaging approach. *J. Hydraul. Engng* **138** (8), 707–725.

DEY, S. & RAIKAR, R. V. 2007 Characteristics of loose rough boundary streams at near-threshold. *J. Hydraul. Engng* **133** (3), 288–304.

DRAZIN, P. G. & REID, W. H. 1981 *Hydrodynamic Stability*. Cambridge University Press.

DYBBS, A. & EDWARDS, R. 1984 A new look at porous media fluid mechanics – Darcy to turbulent. In *Fundamentals of Transport Phenomena in Porous Media* (ed. J. Bear & M. Y. Corapcioglu), pp. 199–256. Martinus Nijhoff Publishers.

FANG, H., BAI, J., HE, G. & ZHAO, H. 2014 Calculations of nonsubmerged groin flow in a shallow open channel by large-eddy simulation. *J. Engng Mech.* **140** (5), 04014016.

FERRARO, D., SERVIDIO, S., CARBONE, V., DEY, S. & GAUDIO, R. 2016 Turbulence laws in natural bed flows. *J. Fluid Mech.* **798**, 540–591.

FRÖHLICH, J. & RODI, W. 2002 Introduction to large eddy simulation of turbulent flows. In *Closure Strategies for Turbulent and Transitional Flows* (ed. B. E. Launder & N. D. Sandham), pp. 197–224. Cambridge University Press.

GERMANO, M., PIOMELLI, U., MOIN, P. & CABOT, W. H. 1991 A dynamic subgrid-scale eddy viscosity model. *Phys. Fluids* **3** (7), 1760–1765.

GHISALBERTI, M. & NEPF, H. M. 2002 Mixing layers and coherent structures in vegetated aquatic flows. *J. Geophys. Res.* **107** (C2), doi:10.1029/2001JC000871.

GIMÉNEZ-CURTO, L. A. & CORNIERO, M. A. 2002 Flow characteristics in the interfacial shear layer between a fluid and a granular bed. *J. Geophys. Res.* **107** (C5), 3044, doi:10.1029/2000JC000729.

GOHARZADEH, A., KHALILI, A. & JØRGENSEN, B. B. 2005 Transition layer thickness at a fluidporous interface. *Phys. Fluids* **17** (5), 057102.

GOYEAU, B., LHUILLIER, D., GOBIN, D. & VELARDE, M. G. 2003 Momentum transport at a fluid-porous interface. *Intl J. Heat Mass Transfer* **46** (21), 4071–4081.

GRASS, A. J., STUART, R. J. & MANSOUR-TEHRANI, M. 1991 Vortical structures and coherent motion in turbulent flow over smooth and rough boundaries. *Phil. Trans. R. Soc. Lond.* A **336** (1640), 33–65.

HAHN, S., JE, J. & CHOI, H. 2002 Direct numerical simulation of turbulent channel flow with permeable walls. *J. Fluid Mech.* **450**, 259–285.

HAN, X., HE, G. & FANG, H. 2017 Double-averaging analysis of turbulent kinetic energy fluxes and budget based on large-eddy simulation. *J. Hydrodyn.* **29** (4), 567–574.

HORTON, N. A. & POKRAJAC, D. 2009 Onset of turbulence in a regular porous medium: an experimental study. *Phys. Fluids* **21** (4), 045104.

JACKSON, P. S. 1981 On the displacement height in the logarithmic velocity profile. *J. Fluid Mech.* **111**, 15–25.

JIMENEZ, J., UHLMANN, M., PINELLI, A. & KAWAHARA, G. 2001 Turbulent shear flow over active and passive porous surfaces. *J. Fluid Mech.* **442**, 89–117.

KHOSRONEJAD, A. & SOTIROPOULOS, F. 2014 Numerical simulation of sand waves in a turbulent open channel flow. *J. Fluid Mech.* **753**, 150–216.

KIM, J., MOIN, P. & MOSER, R. 1987 Turbulence statistics in fully developed channel flow at low Reynolds number. *J. Fluid Mech.* **177**, 133–166.

https://doi.org/10.1017/jfm.2018.314 Published online by Cambridge University Press

KIRONOTO, B. A. & GRAF, W. H. 1994 Turbulence characteristics in rough uniform open-channel flow. *Proc. Inst. Civ. Engrs Wat., Marit. Energy* **106** (4), 333–334.

KOLMOGOROV, A. N. 1941 The local structure of turbulence in incompressible viscous fluids at very large Reynolds numbers. *Dokl. Akad. Nauk SSSR* **30**, 299–303.

KONG, F. Y. & SCHETZ, J. A. 1982 Turbulent boundary layer over porous surfaces with different surface geometries. In *AIAA Paper* 82-0030, 1–10.

KROGSTAD, P. Å. & ANTONIA, R. A. 1999 Surface roughness effects in turbulent boundary layers. *Exp. Fluids* **27** (5), 450–460.

KUWATA, Y. & SUGA, K. 2016 Lattice Boltzmann direct numerical simulation of interface turbulence over porous and rough walls. *Intl J. Heat Fluid Flow* **61** (October), 145–157.

LIU, Q. & PROSPERETTI, A. 2011 Pressure-driven flow in a channel with porous walls. *J. Fluid Mech.* **679**, 77–100.

LOPEZ, F. & GARCIA, M. H. 1999 Wall similarity in turbulent open channel flow. *J. Engng Mech.* **125** (7), 789–796.

LU, S. S. & WILLMARTH, W. W. 1973 Measurements of the structure of the Reynolds stress in a turbulent boundary layer. *J. Fluid Mech.* **60**, 481–511.

MANES, C., POGGI, D. & RIDOLFI, L. 2011 Turbulent boundary layers over permeable walls: scaling and near-wall structure. *J. Fluid Mech.* **687**, 141–170.

MANES, C., POKRAJAC, D. & MCEWAN, I. 2007 Double-averaged open-channel flows with small relative submergence. *J. Hydraul. Engng* **133** (8), 896–904.

MANES, C., POKRAJAC, D., MCEWAN, I. & NIKORA, V. 2009 Turbulence structure of open channel flows over permeable and impermeable beds: a comparative study. *Phys. Fluids* **21** (12), 125109.

MIGNOT, E., BARTHELEMY, E. & HURTHER, D. 2009*a* Double-averaging analysis and local flow characterization of near-bed turbulence in gravel-bed channel flows. *J. Fluid Mech.* **618** (January), 279–303.

MIGNOT, E., HURTHER, D. & BARTHELEMY, E. 2009*b* On the structure of shear stress and turbulent kinetic energy flux across the roughness layer of a gravel-bed channel flow. *J. Fluid Mech.* **638** (November), 423–452.

NEZU, I. 2005 Open-channel flow turbulence and its research prospect in the 21st century. *J. Hydraul. Engng* **131** (4), 229–246.

NEZU, I. & NAKAGAWA, H. 1993 *Turbulence in Open-Channel Flows*. A. A. Balkema.

NIKORA, V. & GORING, D. 2000 Flow turbulence over fixed and weakly mobile gravel beds. *J. Hydraul. Engng* **126** (9), 679–690.

NIKORA, V., GORING, D., MCEWAN, I. & GRIFFITHS, G. 2001 Spatially averaged open-channel flow over rough bed. *J. Hydraul. Engng* **127** (2), 123–133.

NIKORA, V., MCEWAN, I., MCLEAN, S., COLEMAN, S., POKRAJAC, D. & WALTERS, R. 2007*a* Double-averaging concept for rough-bed open-channel and overland flows: theoretical background. *J. Hydraul. Engng* **133** (8), 873–883.

NIKORA, V., MCLEAN, S., COLEMAN, S., POKRAJAC, D., MCEWAN, I., CAMPBELL, L., ABERLE, J., CLUNIE, D. & KOLL, K. 2007*b* Double-averaging concept for rough-bed open-channel and overland flows: applications. *J. Hydraul. Engng* **133** (8), 884–895.

NIKORA, V. I. & SMART, G. M. 1997 Turbulence characteristics of New Zealand gravel-bed rivers. *J. Hydraul. Engng* **123** (9), 764–773.

PESKIN, C. S. 1972 Flow patterns around heart valves: a numerical method. *J. Comput. Phys.* **10** (2), 252–271.

POKRAJAC, D., CAMPBELL, L. J., NIKORA, V., MANES, C. & MCEWAN, I. 2007 Quadrant analysis of persistent spatial velocity perturbations over square-bar roughness. *Exp. Fluids* **42** (3), 413–423.

RAUPACH, M. R., ANTONIO, R. A. & RAJAGOPALAN, S. 1991 Rough-wall turbulent boundary layers. *Appl. Mech. Rev.* **44**, 1–25.

ROSGEN, D. L. 1994 A classification of natural rivers. *Catena* **22** (3), 169–199.

SARKAR, S. & DEY, S. 2010 Double-averaging turbulence characteristics in flows over a gravel-bed. *J. Hydraul. Res.* **48** (6), 801–809.

https://doi.org/10.1017/jfm.2018.314 Published online by Cambridge University Press

SARKAR, S., PAPANICOLAOU, A. N. & DEY, S. 2016 Turbulence in gravel-bed stream with an array of large gravel obstacles. *J. Hydraul. Engng* **142** (11), 04016052.

SINGH, K. M., SANDHAM, N. D. & WILLIAMS, J. J. R. 2007 Numerical simulation of flow over a rough bed. *J. Hydraul. Engng* **133** (4), 386–398.

SMART, G. M. & HABERSACK, H. M. 2007 Pressure fluctuations and gravel entrainment in rivers. *J. Hydraul. Res.* **45** (5), 661–673.

SONG, T. & GRAF, W. H. 1994 Nonuniform open-channel flow over a rough bed. *J. Hydrosci. Hydraul. Engng* **12** (1), 1–25.

SUGA, K. 2016 Understanding and modelling turbulence over and inside porous media. *Flow Turbul. Combust.* **96** (3), 717–756.

SUGA, K., MATSUMURA, Y., ASHITAKA, Y., TOMINAGA, S. & KANEDA, M. 2010 Effects of wall permeability on turbulence. *Intl J. Heat Fluid Flow* **31** (6), 974–984.

SUGA, K., MORI, M. & KANEDA, M. 2011 Vortex structure of turbulence over permeable walls. *Intl J. Heat Fluid Flow* **32** (3), 586–595.

TOWNSEND, A. A. 1976 *The Structure of Turbulent Shear Flow*. Cambridge University Press.

VANDERWEL, C. & GANAPATHISUBRAMANI, B. 2015 Effects of spanwise spacing on large-scale secondary flows in rough-wall turbulent boundary layers. *J. Fluid Mech.* **774**, R2.

VOERMANS, J. J., GHISALBERTI, M. & IVEY, G. N. 2017 The variation of flow and turbulence across the sediment–water interface. *J. Fluid Mech.* **824**, 413–437.

WHITAKER, S. 1996 The Forchheimer equation: a theoretical development. *Transp. Porous Med.* **25** (1), 27–61.

WILSON, A. M., HUETTEL, M. & KLEIN, S. 2008 Grain size and depositional environment as predictors of permeability in coastal marine sands. *Estuar. Coast. Shelf Sci.* **80** (1), 193–199.

WILSON, N. R. & SHAW, R. H. 1977 A higher order closure model for canopy flow. *J. Appl. Meteorol.* **16** (11), 1197–1205.

YUAN, J. & PIOMELLI, U. 2014 Roughness effects on the Reynolds stress budgets in near-wall turbulence. *J. Fluid Mech.* **760**, R1.

ZAGNI, A. F. E. & SMITH, K. V. H. 1976 Channel flow over permeable beds of graded spheres. *J. Hydraul. Div.* **102** (2), 207–222.

ZIPPE, H. J. & GRAF, W. H. 1983 Turbulent boundary-layer flow over permeable and non-permeable rough surfaces. *J. Hydraul. Res.* **21** (1), 51–65.

https://doi.org/10.1017/jfm.2018.314 Published online by Cambridge University Press